Particles and the Cosmos

2019/2020

Sascha Caron, Jörg Hörandel

NM109
first semester, 6 ec

32 hrs lecture Wednesday 10:30 - 12:15 HG 00.086
32 hrs problem session Thursday 13:30 - 15:15 HG 02.052

Lectures:

Experimental methods (JRH)
04.09.2019 1. Interactions with matter
11.09.2019 2. Detectors

Standard model (SC)
18.09.2019 3. Particles, QED, Feynman rules
25.09.2019 4. Hadrons and QCD
02.10.2019 5. Hadrons and QCD
09.10.2019 6. Weak interactions, CP violation
16.10.2019 7. Higgs mechanism

Astroparticle physics (JRH)
06.11.2019 8. The birth of cosmic rays
13.11.2019 9. Cosmic rays in the Galaxy, in the heliosphere, and the Earth magnetic field
20.11.2019 10. Cosmic rays at the top of and in the atmosphere
27.11.2019 11. Cosmic rays underground - neutrino oscillations
04.12.2019 12. Neutrino oscillations, Astroparticle Physics

Beyond the Standard Model, Dark Matter (SC)
11.12.2019 13. Lambda CDM, Big-bang nucleosynthesis
18.12.2019 14. Dark matter - Beyond-the-standard-model reasons

for Astroparticle Physics

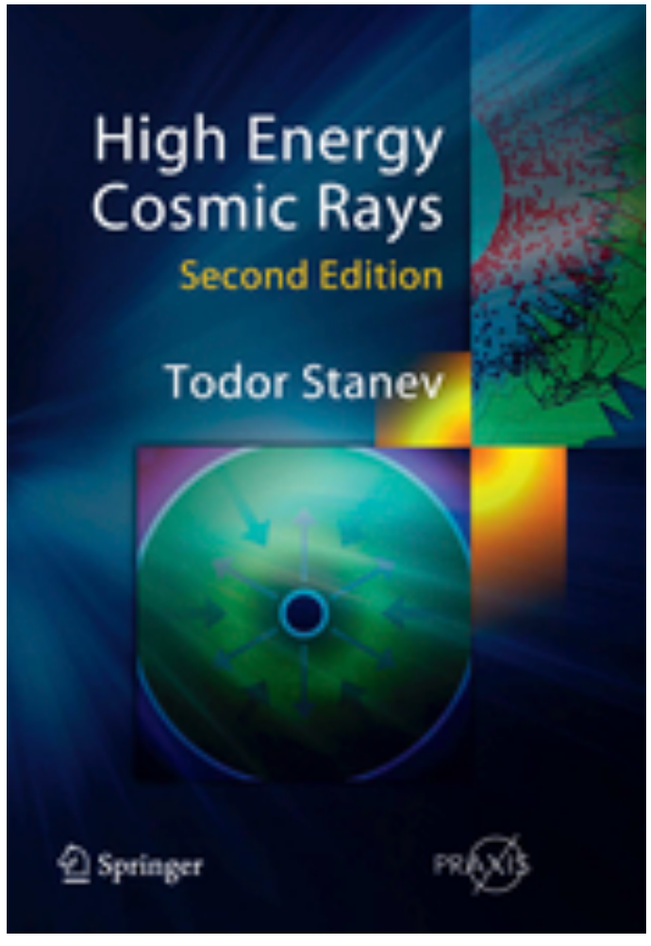

Jörg R. Hörandel
HG 02.721
http://particle.astro.ru.nl

Rafael Alves Batista
email: r.batista@astro.ru.nl

birth of cosmic rays
CRs: supernova remnants
neutrinos: e.g. Sun (lecture 8)

propagation of CRs in the Galaxy
interactions with ISM (lecture 9)

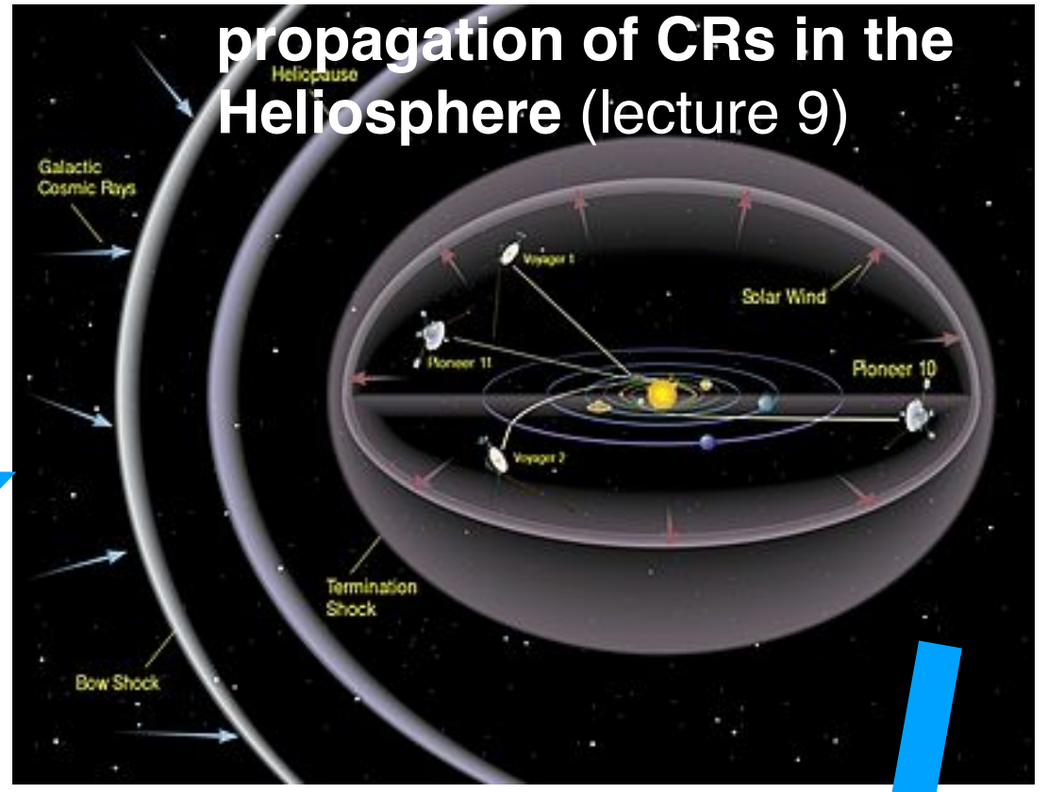

propagation of CRs in the Heliosphere (lecture 9)

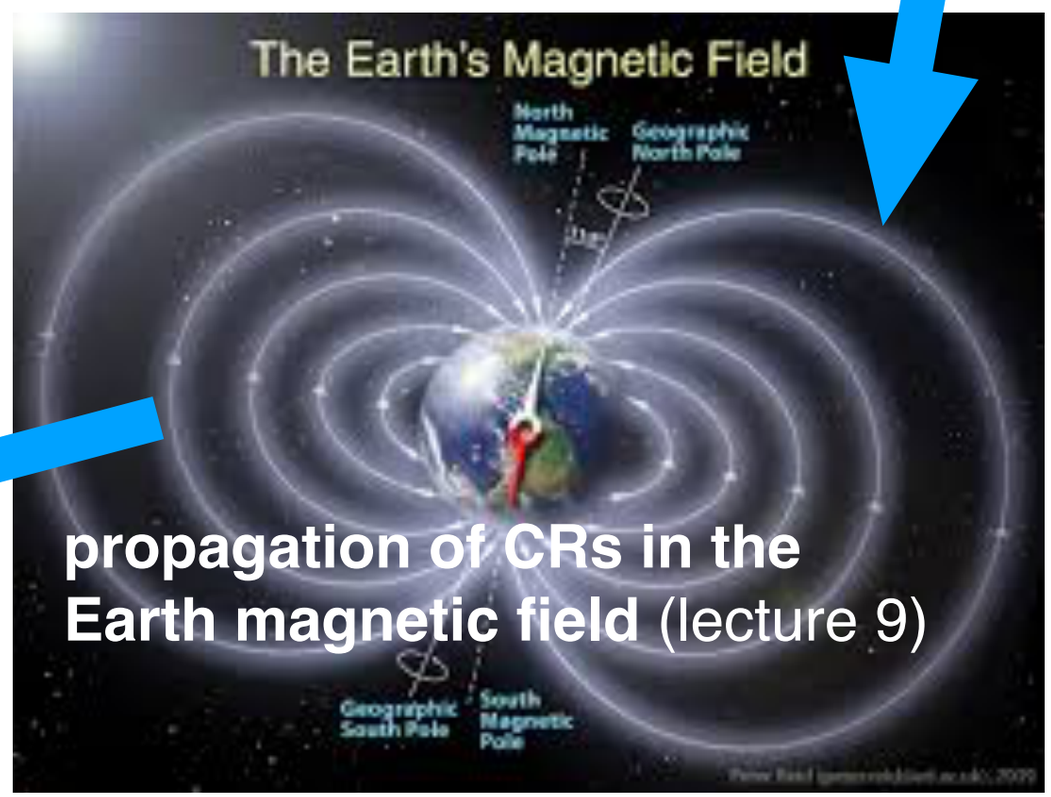

propagation of CRs in the Earth magnetic field (lecture 9)

CRs at the top of the atmosphere (lecture 10)

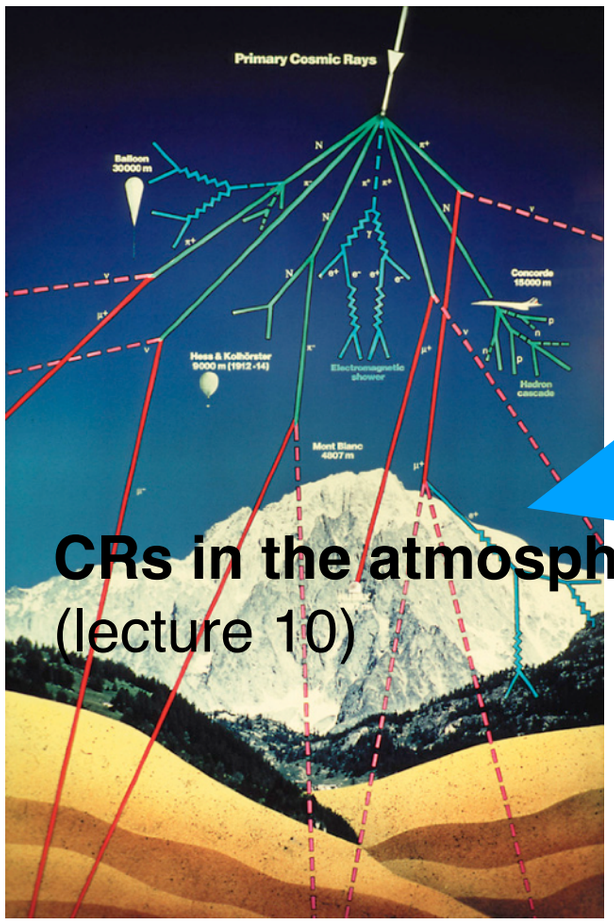

CRs in the atmosphere (lecture 10)

CRs underground (lecture 11)
neutrino oscillations (lecture 11+12)

today:
Stanev, chapter 5

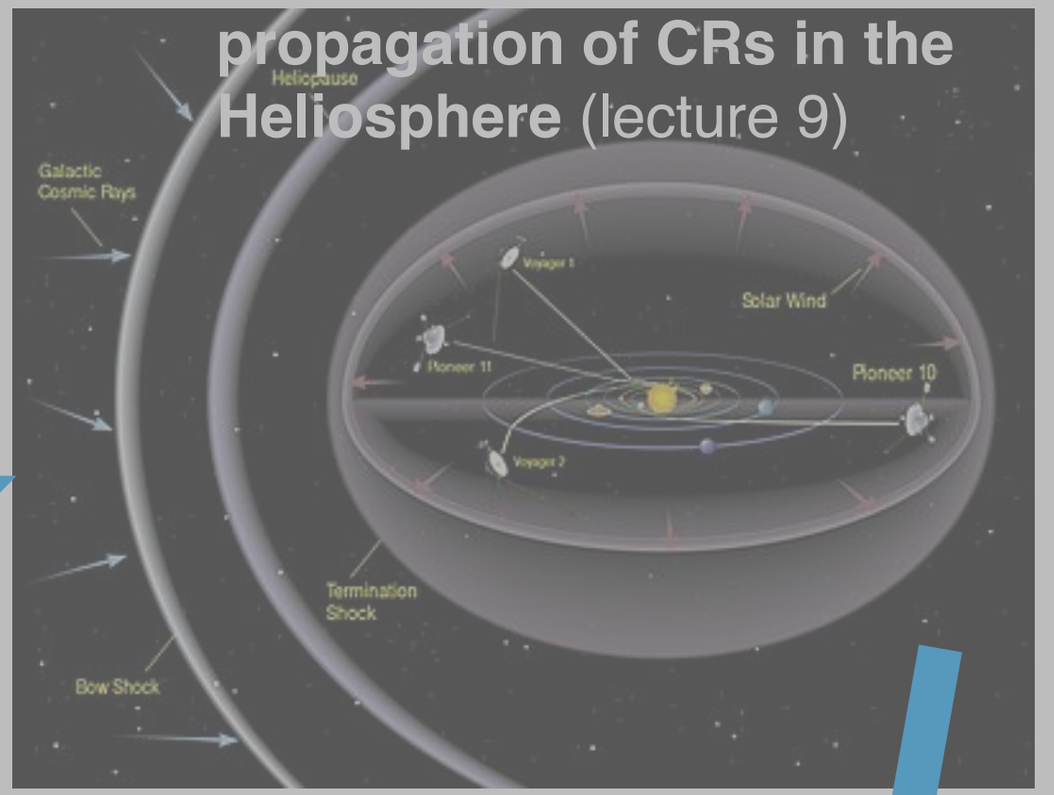

propagation of CRs in the Heliosphere (lecture 9)

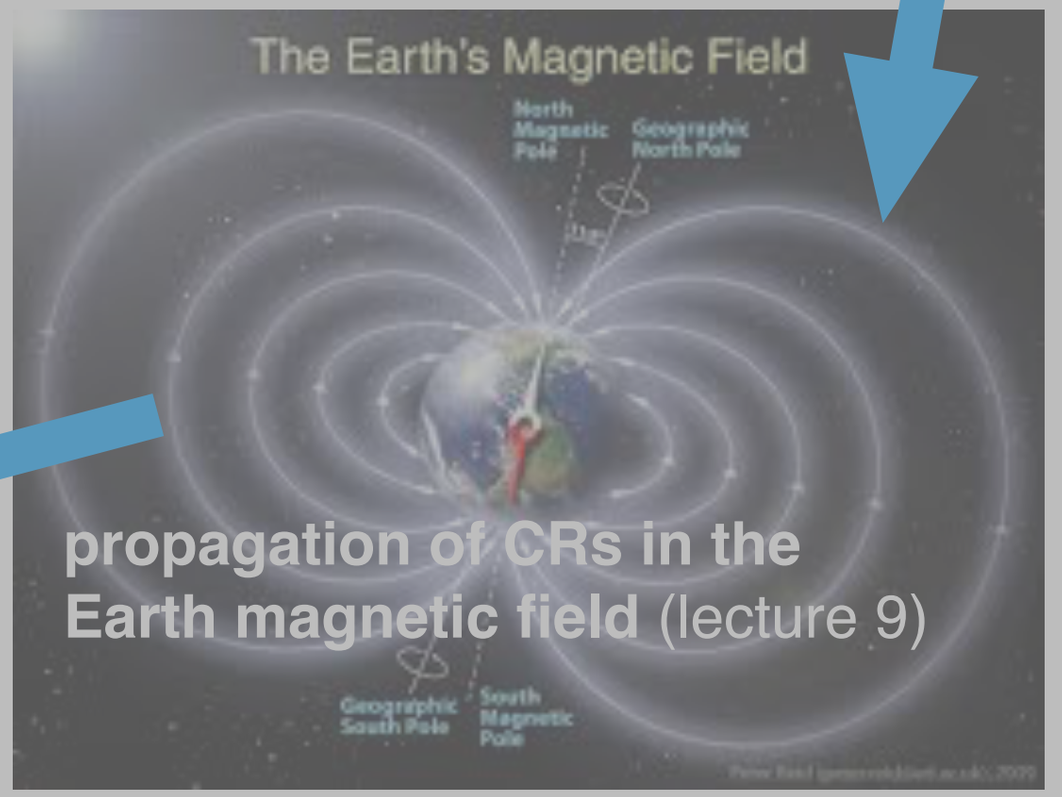

propagation of CRs in the Earth magnetic field (lecture 9)

CRs at the top of the atmosphere (lecture 10)

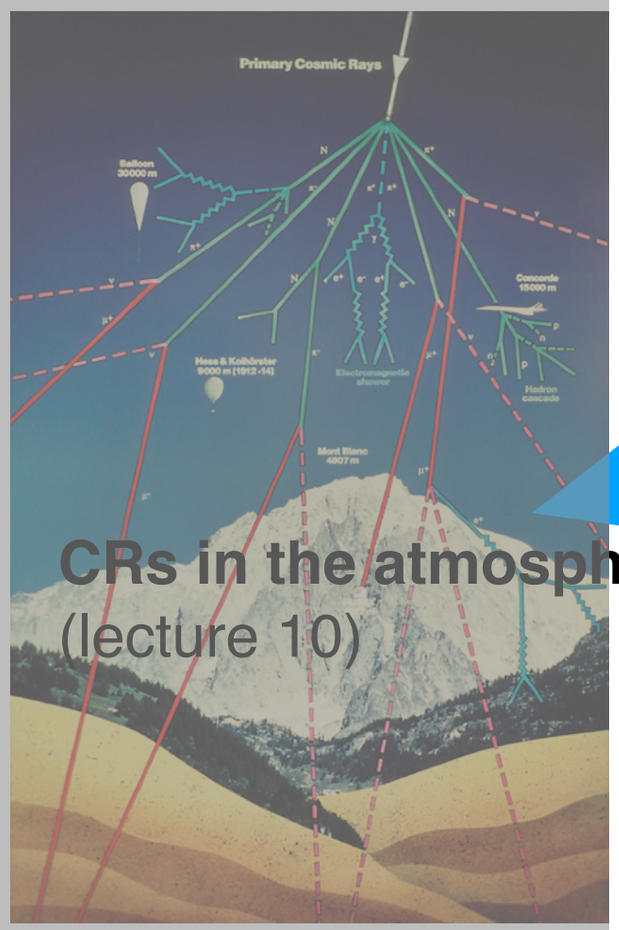

CRs in the atmosphere (lecture 10)

CRs underground (lecture 11)
neutrino oscillations (lecture 11+12)

Detectors for direct measurements of Cosmic Rays above the atmosphere

•Silicon detector	IZI, A, E	isotopes
•Magnet spectrometer	+/- Z, E	anti-particles
•Calorimeter	IZI, E	elements
•Cherencov detector	IZI, E	elements
•Transition radiation detector	IZI, E	elements

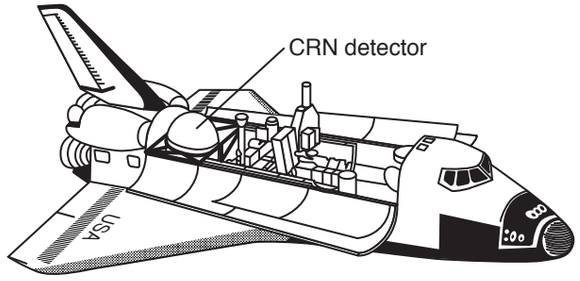

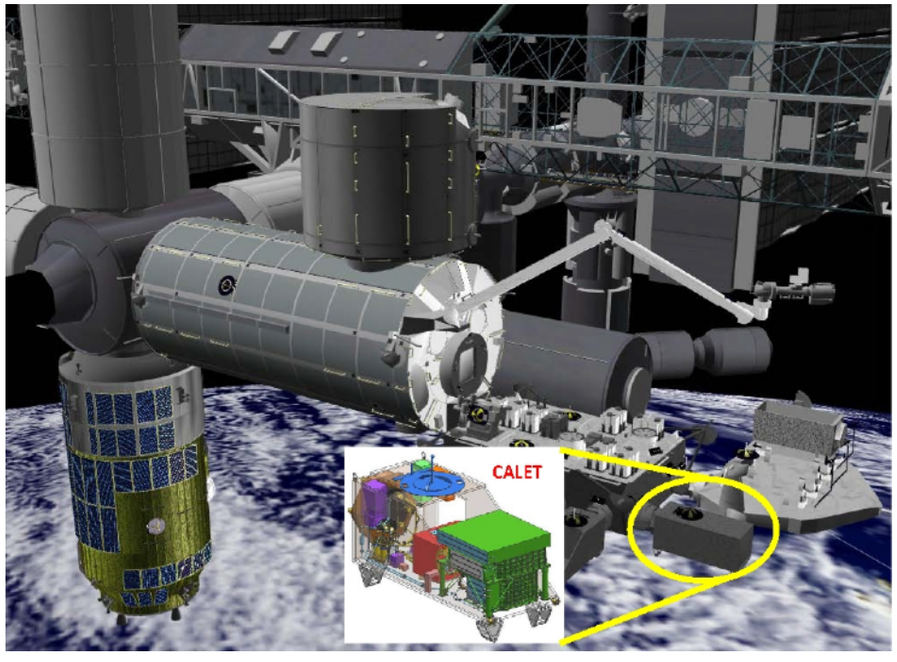

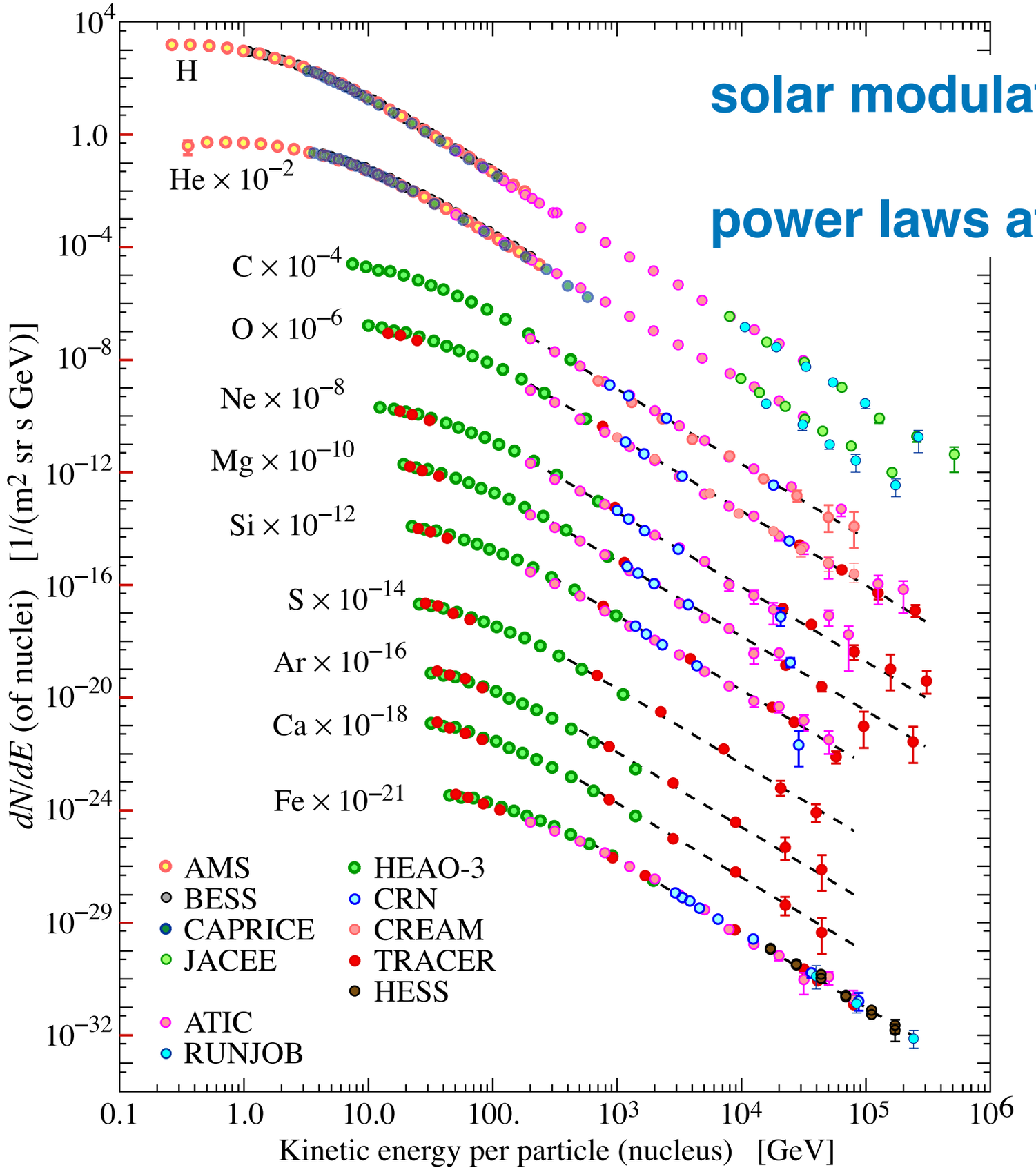

solar modulation at low energies

power laws at high energies

$$\frac{dN}{dE} \propto E^{\gamma}$$

Figure 24.1: Major components of the primary cosmic radiation from Refs. [1–12 The figure was created by P. Boyle and D. Muller. Color version at end of book.

Properties of Cosmic Rays E<10^{14} eV

most important properties:

1. **energy spectra are power laws**
   --> non-thermal origin $\left(\frac{dN}{dE} \propto e^{-\kappa E}\right)$

$$\frac{dN}{dE} \propto E^{\gamma} \quad \gamma \approx -2.7$$

2. **below ~10 GV energy spectra deviate from power laws**
   --> solar modulation, charged particles of extra-solar origin (galactic origin) drift against the solar wind towards Earth/solar system

   magnetic rigidity $R = \frac{p \cdot c}{Z \cdot e}$

3. **in first approximation all elements exhibit about the same slope**
   spectral index $\gamma \approx -2.7$

Cosmic ray spectra and composition

The cosmic ray fluxes of the different groups of nuclei are fit with the expression

$$F(E_k) = K\left[E_k + B\exp\left(-\frac{C}{\sqrt{E_k}}\right)\right]^{-\alpha}, \tag{5.6}$$

where the coefficients B, C express the kinematic change of the shape of the cosmic ray spectrum expressed in kinetic energy.

Table 5.1. Fit parameters for hydrogen. Data sets are marked as follows: 1, all 11 data sets; 2, AMS, BESS, Ryan et al. + TeV data; 3, AMS, BESS only; 4, LEAP, IMAX, CAPRICE94, MASS91 + TeV data.

Fit #	α	K	B	C	χ^2/n.d.f.
1	2.68 ± 0.04	9646 ± 1100	2.11	0.45	153.0
2	2.74 ± 0.01	14500 ± 360	2.20	0.25	1.03
3	2.74 ± 0.01	14510 ± 560	2.21	0.25	0.27
4	2.68 ± 0.05	9345 ± 1500	2.12	0.48	246.0

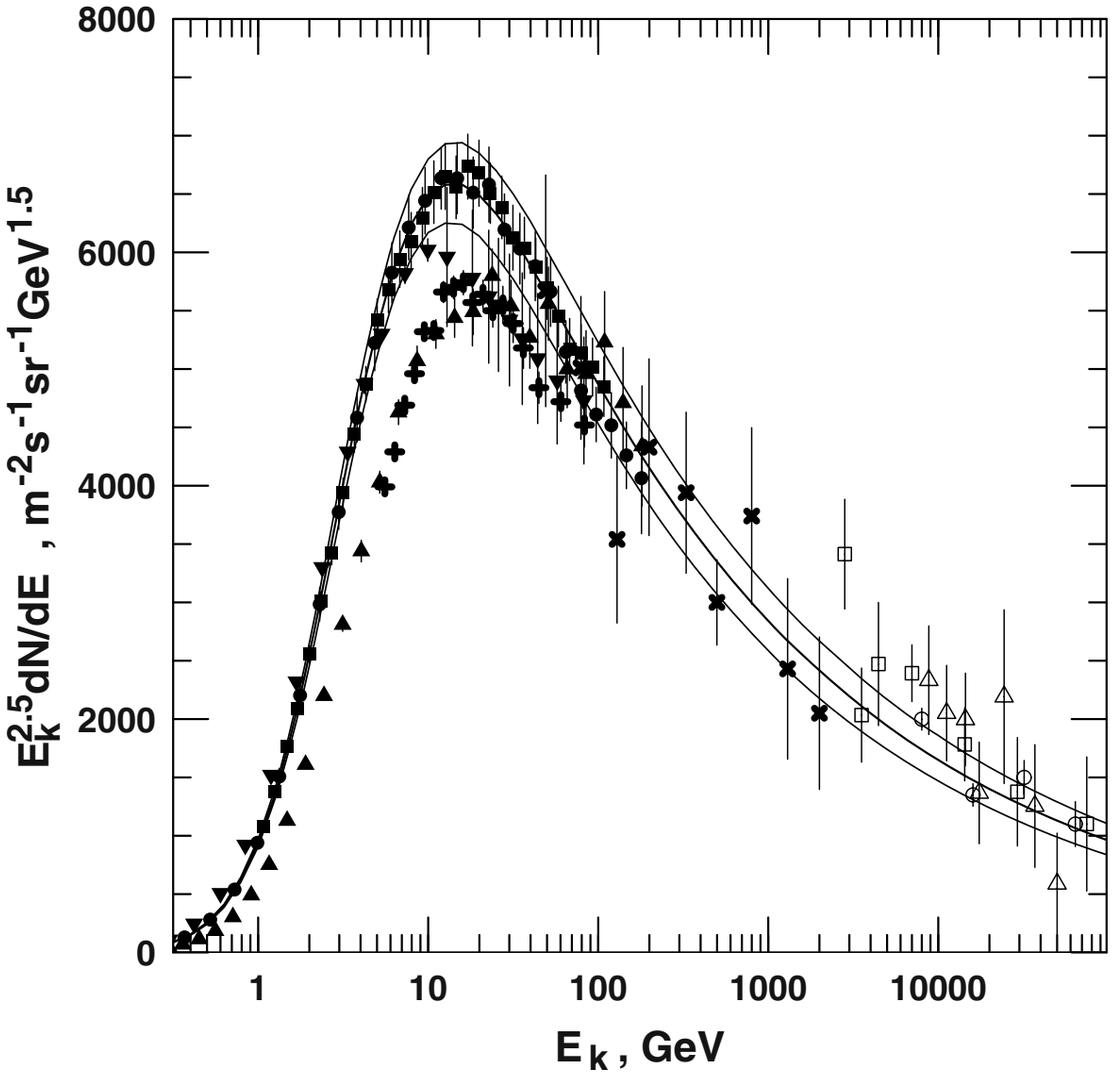

proton/hydrogen spectra

Fig. 5.11. Comparison of all hydrogen data sets to the fits 2 and 3. The thick line shows the central value of the fit, and the thin lines use the errors of K and α to show the maximum and minimum fluxes allowed by the fit.

Table 5.3. Fit parameters for helium data sets are marked as follows: 1, all 11 data sets; 2, all excluding BESS; 3, all excluding CAPRICE94; 4, no TeV data.

fit #	α	K	B	C	χ^2/n.d.f.
1	2.60 ± 0.02	426 ± 31	1.22	0.42	7.00
2	2.61 ± 0.02	426 ± 34	1.22	0.43	7.95
3	2.61 ± 0.02	434 ± 36	1.20	0.41	7.40
4	2.63 ± 0.04	462 ± 56	1.22	0.37	7.86

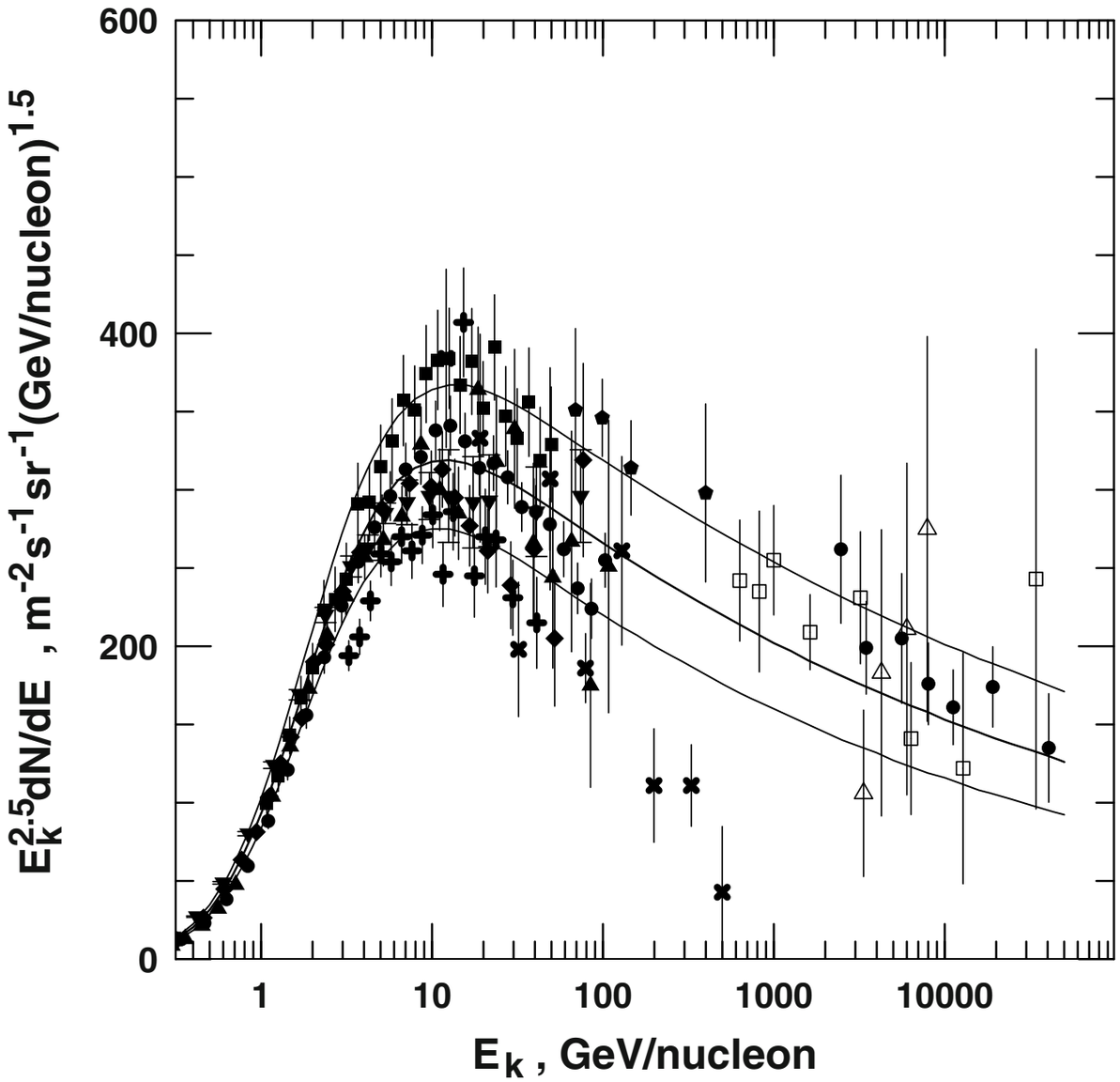

helium spectra

Fig. 5.12. Fit of the helium flux. Symbols are as in Fig. 5.11. The results of the RICH experiment are shown with filled pentagons.

heavier elements

Table 5.5. Fit parameters for heavier nuclei. For each group there are three fitting sets, that include all data sets, the 'high' data sets and the 'low' data sets.

fit #	γ	K	B	C	χ^2/n.d.f.
CNO					
all	2.68 ± 0.06	37.1 ± 6	21.2	1.67	13.9
high	2.60 ± 0.07	33.2 ± 5	0.97	0.01	2.52
low	2.71 ± 0.09	38.8 ± 9	36	1.95	19.0
SiMg					
all	2.78 ± 0.08	18.4 ± 4	3.10	0.40	2.66
high	2.79 ± 0.08	34.2 ± 6	2.14	0.01	0.74
low	2.80 ± 0.07	18.6 ± 6	5.08	0.59	1.81
z >17					
all	2.75 ± 0.04	4.70 ± 0.75	5.35	0.74	2.15
high	2.68 ± 0.01	4.45 ± 0.50	3.07	0.41	0.54
low	2.84 ± 0.04	5.71 ± 1.10	6.20	0.78	1.62

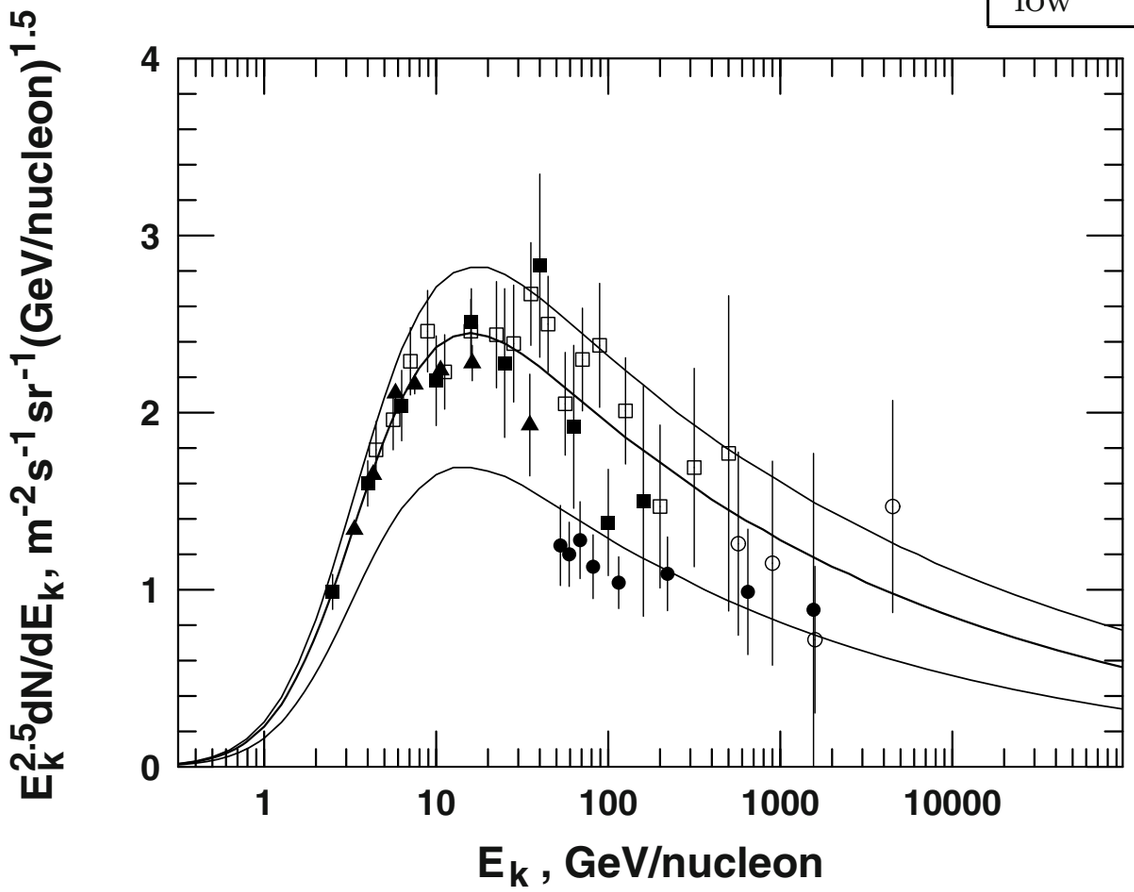

Fig. 5.13. Fit of the z >17 flux. HEAO-3 data are shown with filled triangles, Simon et al. with filled squares, CRN with filled circles, JACEE with open circles and Ichimura et al. with open squares.

relative contribution of different elements in cosmic rays

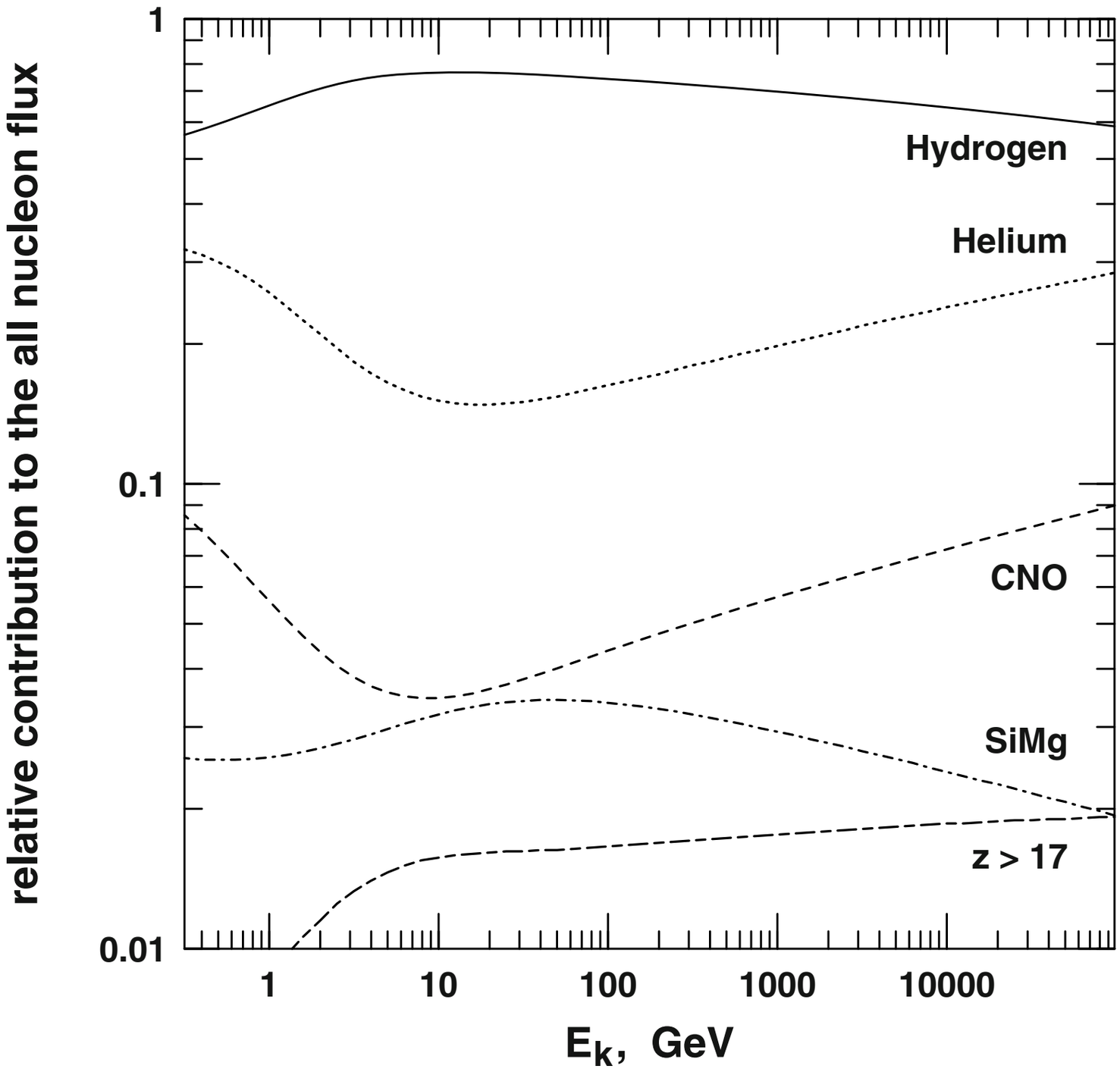

Fig. 5.14. Relative contribution of different groups of nuclei to the all nucleon flux. The 'high' fits from the previous section are used for heavy nuclei. Average mass numbers of 1, 2, 14, 26, and 56 are assumed – see text.

more recent data

Direct measurements of proton and He spectra

❑ **PAMELA detected a spectral break in PROTON and HE spectra at R ~ 240 GV**

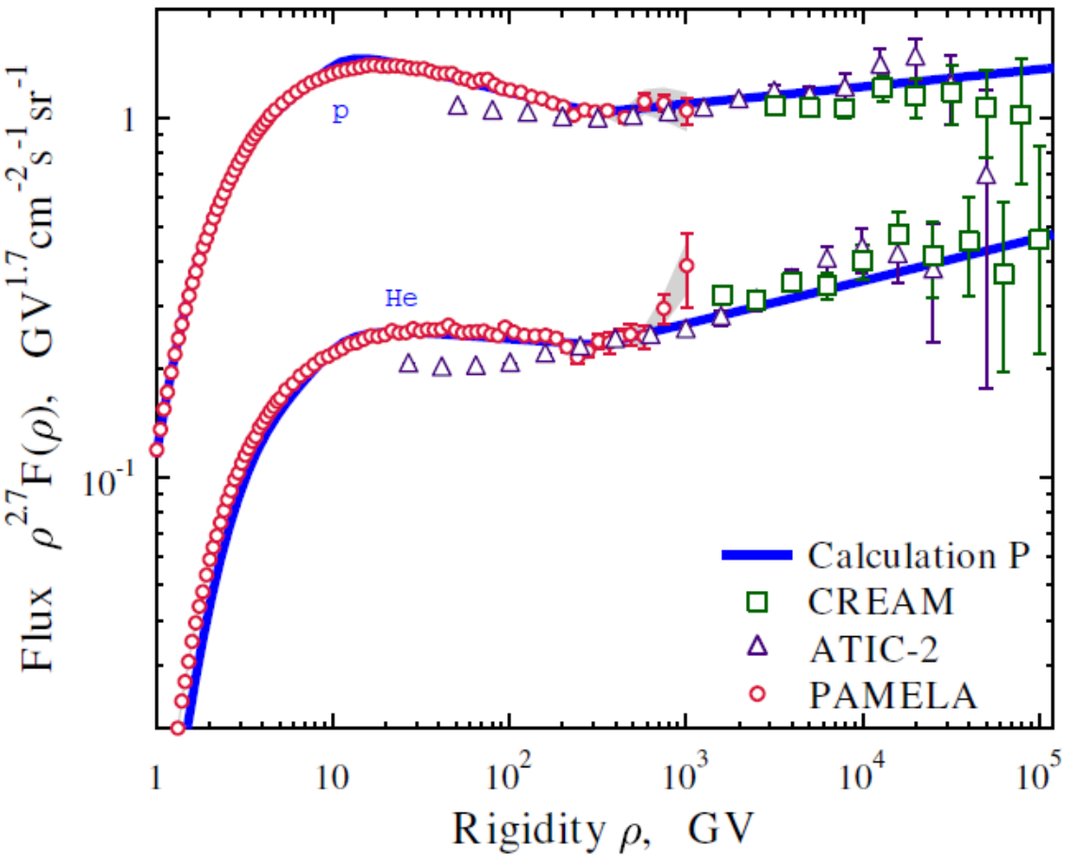

<u>A single power-law seems inadequate to fit the spectra</u>

The slope of Z>2 NUCLEI at high energy looks similar to He and different from protons

❑ **The break also appears in the spectra of NUCLEI measured by CREAM up to several TeV/n**

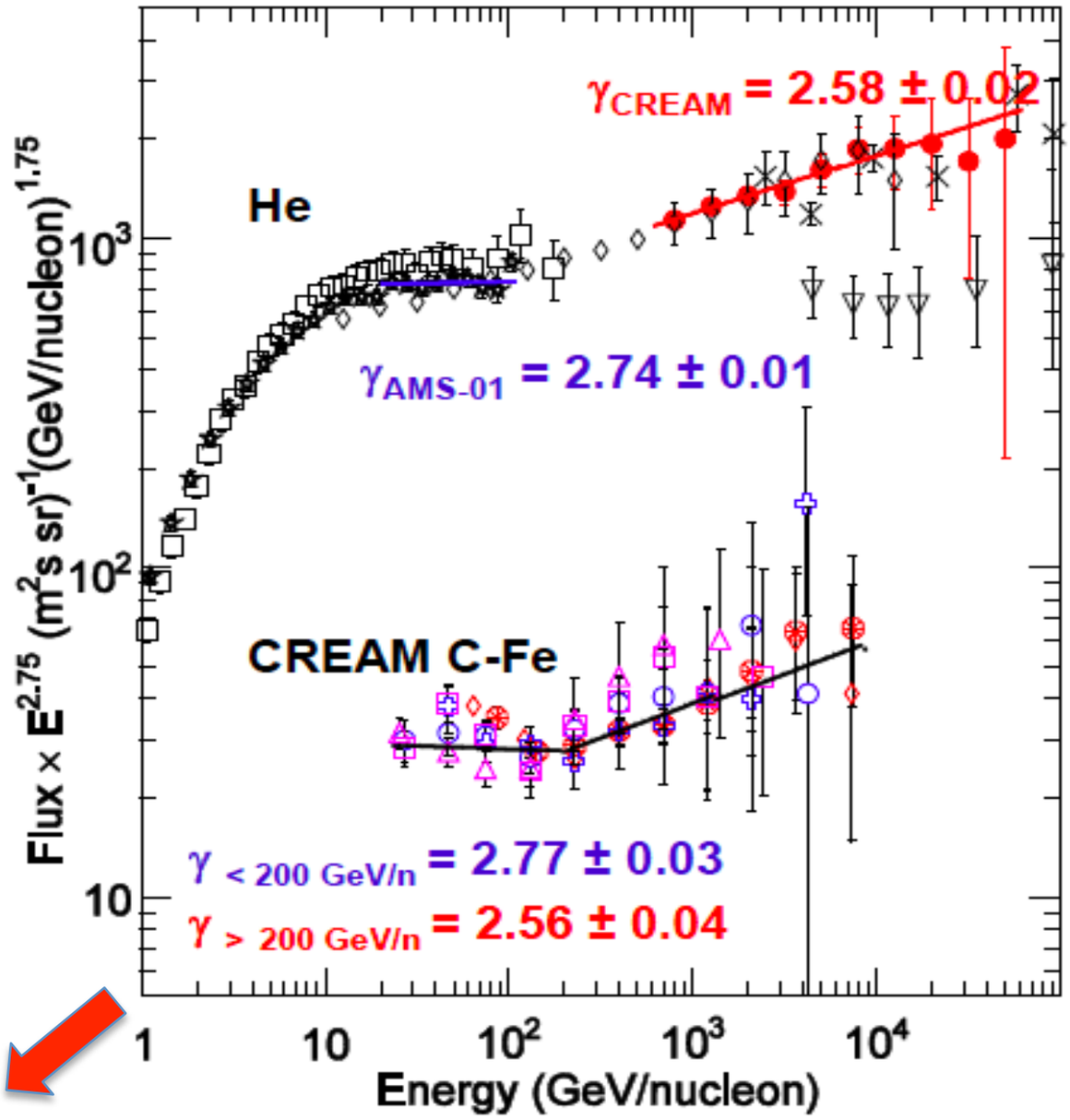

Ahn et al. ApJ 714, L89, 2010
Yoon et al. ApJ **728**, *122*, 2011

PAMELA: Proton and Helium Nuclei Spectra & H/He ratio

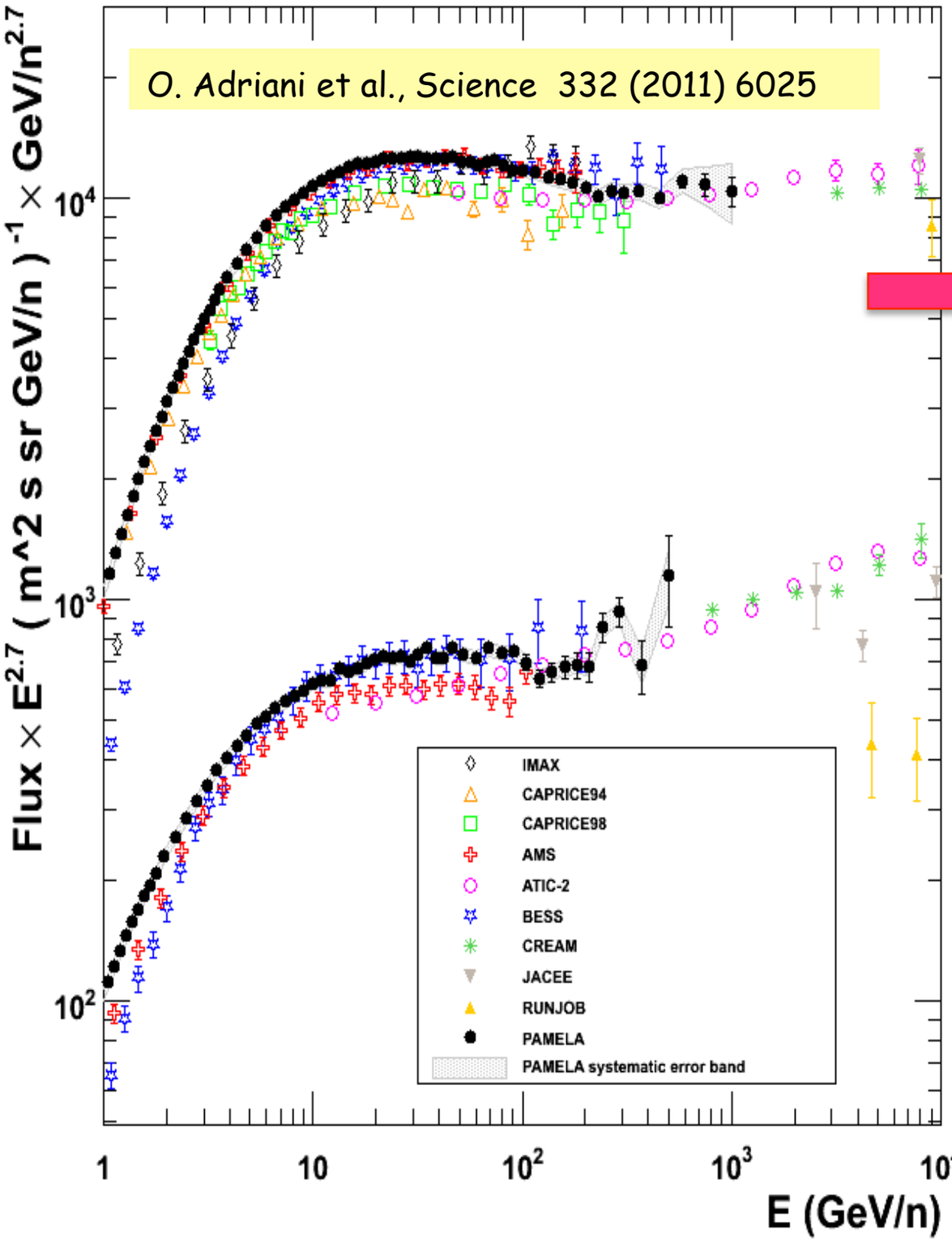

- **First high-statistics and high-precision measurement over three decades in energy**
- Deviations from single power law (SPL):
  - Spectra gradually soften in the range 30÷230GV
  - Spectral hardening @ R~235GV
    $\Delta\gamma \sim 0.2 \div 0.3$
    Single power-law rejected at 98% CL

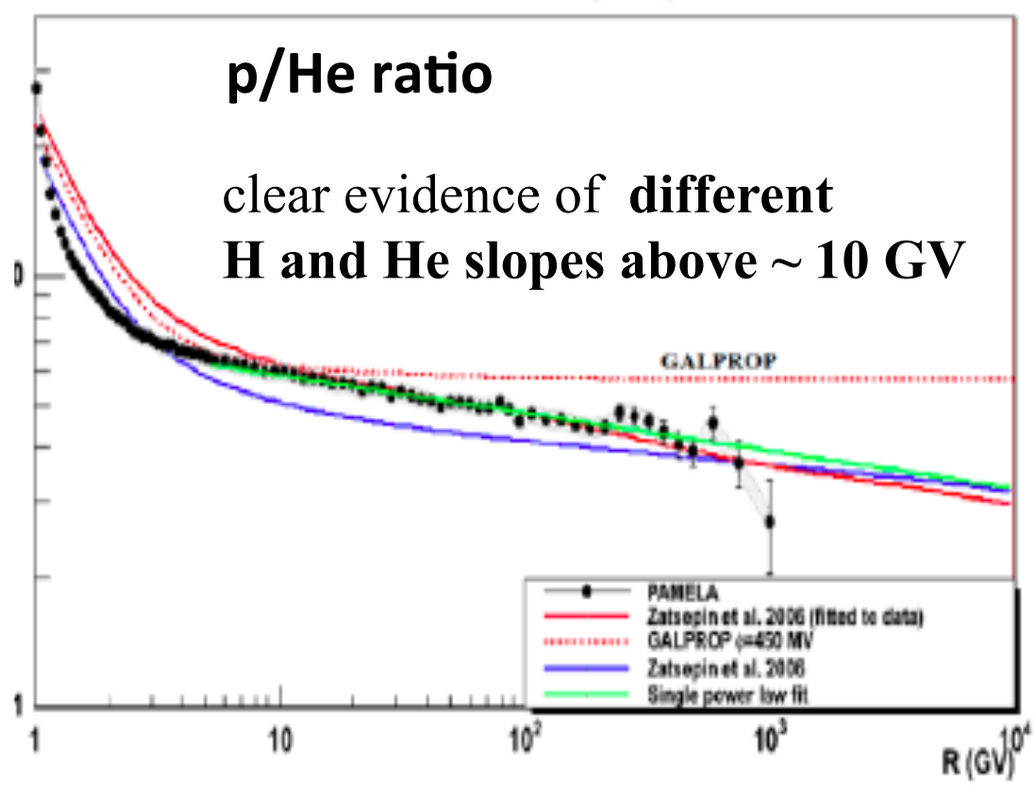

Proton and Helium:

✧ need to extend precision measurements to the multi-TeV region

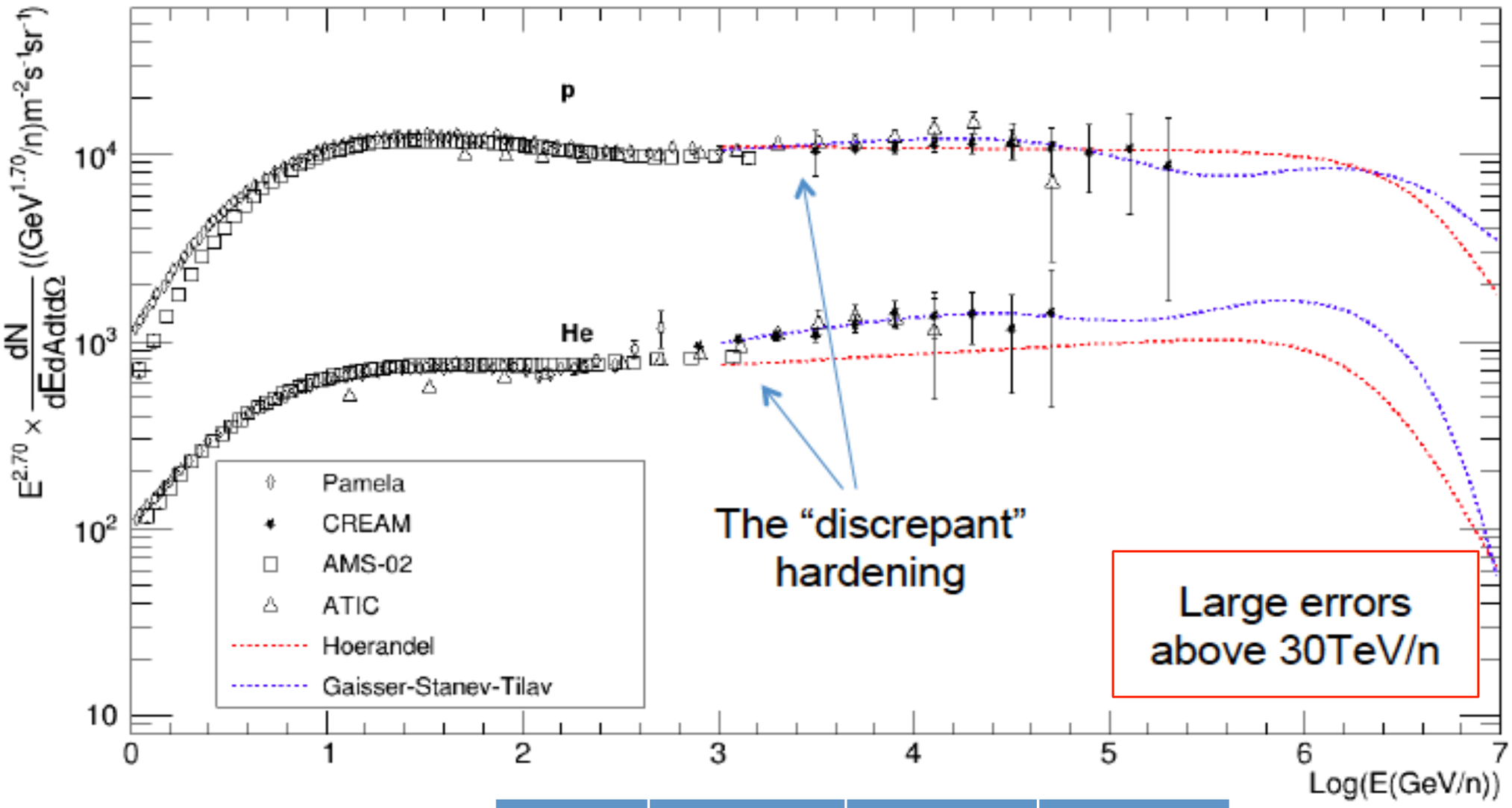

fitted slope of p, He spectra above 230 GV

	fit range p (He)	γ_p	γ_{He}
CREAM(*)	2.5 -250 TeV	-2.66±0.02	-2.58 ±0.02
PAMELA	> 230 (250) GV	-2.706±0.07	-2.604±0.08
AMS-02	> 330 (250) GV	-2.702±0.01	-2.639±0.01

(*) Ahn et al., ApJ **714**, *L89*, 2010

TRACER: Energy spectra for individual elements

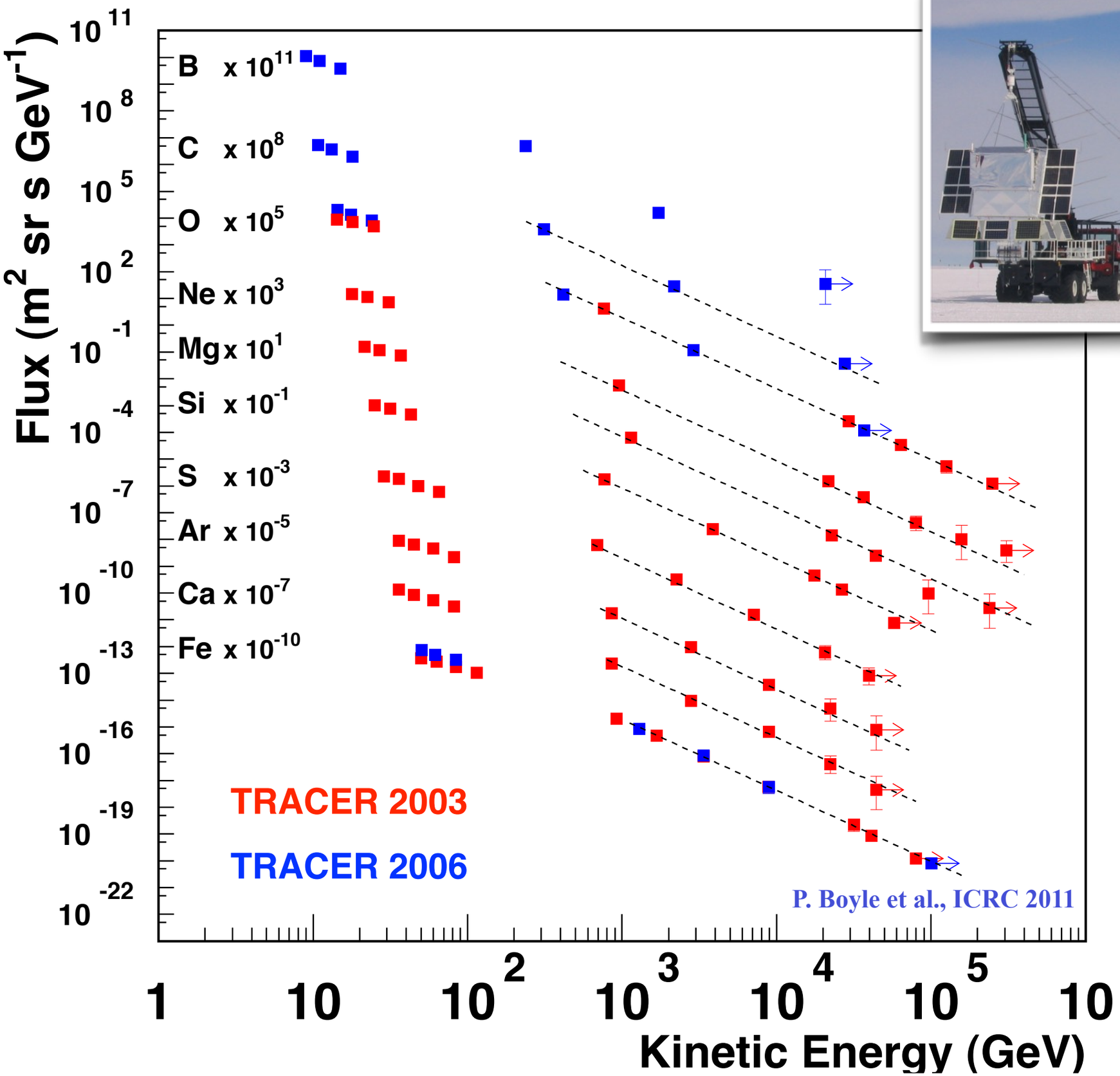

A. Obermeier et al., ApJ 752 (2012) 69

the boron-to-carbon ratio

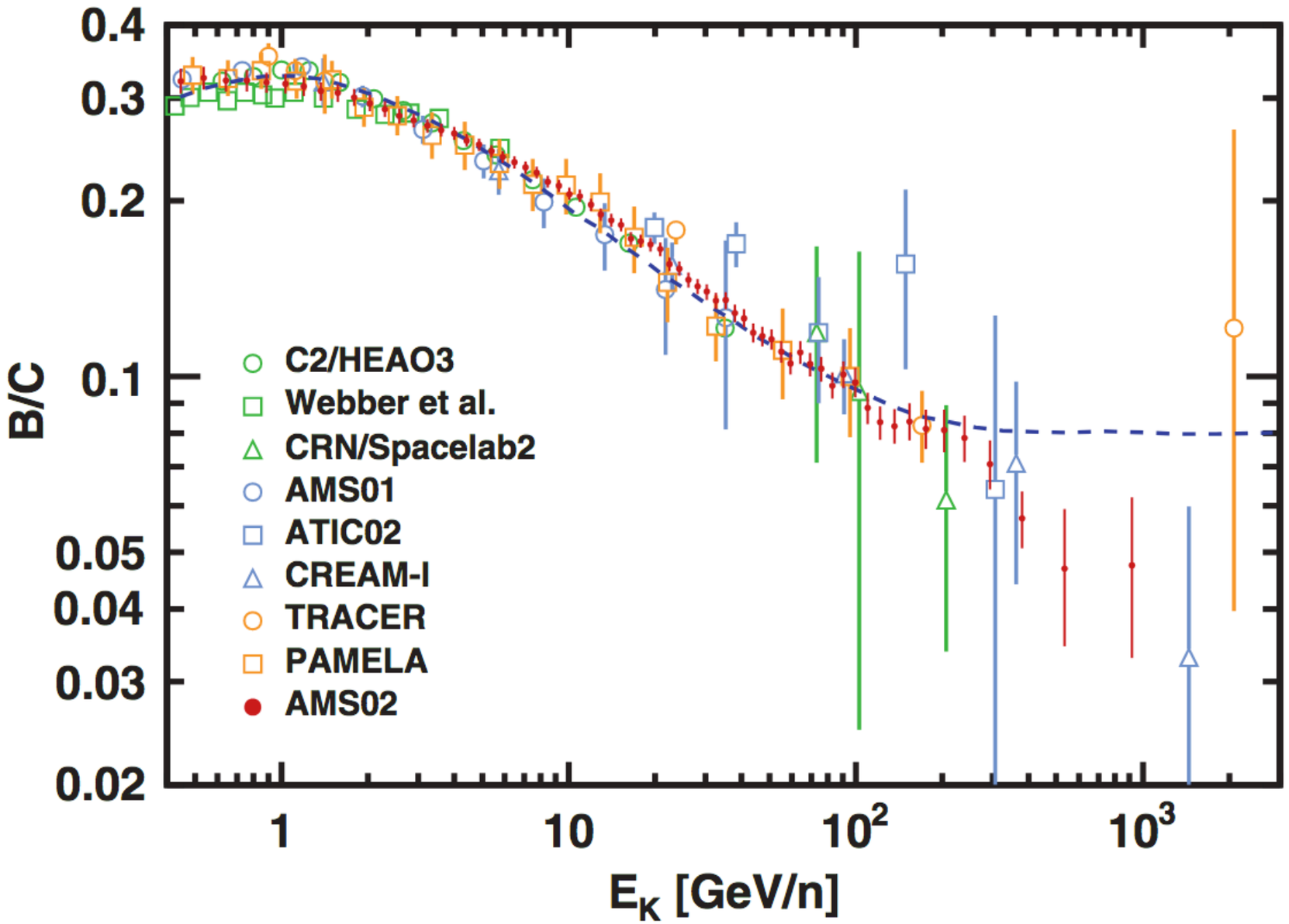

- featureless B/C ratio
- best fit compatible Kolmogorov turbulence

Relative abundance of elements at Earth

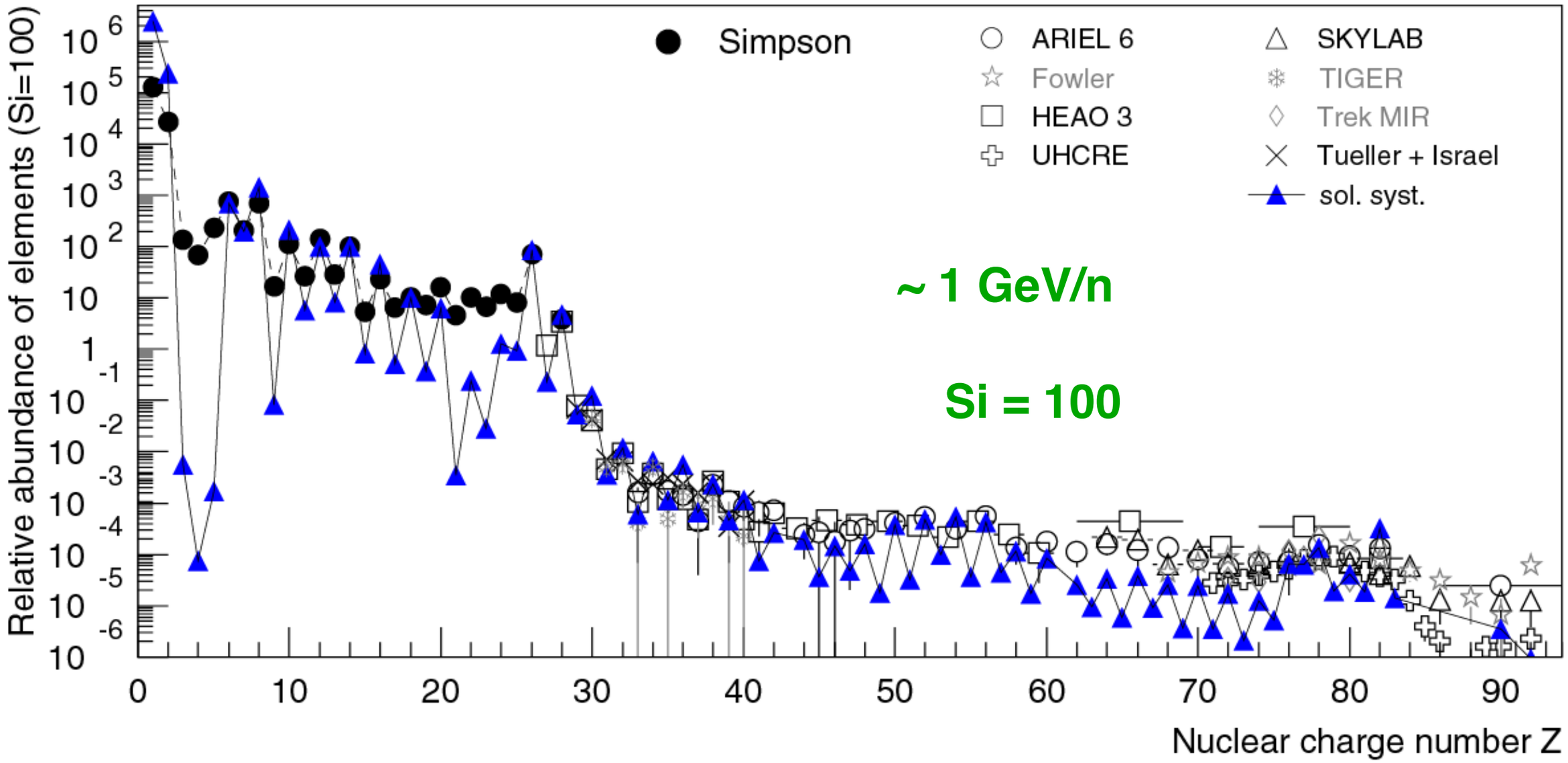

→ **Cosmic rays are „regular matter“, accelerated to extremely high energies**

JRH, Adv. Space Res. 41 (2008) 442

elemental composition of cosmic rays

~89% p
9% He
1% heavy nuclei
} ~1 GeV/n

~1% electrons/positrons
<0.1% gamma rays

some remarks:

1. even-odd effect
--> due to high binding energy of ee-nuclei

2. elements Li, Be, B are more abundant in CRs than in solar system
--> propagation in Galaxy

3. same effect for sub-Fe elements (~Ca - Fe)

4. p + He are less abundant in CRs as compared to solar system

electrons(+positrons): ~1% of nuclear cosmic rays

energy spectrum is steeper

$$\frac{dN}{dE} \propto E_e^{-3.3}$$

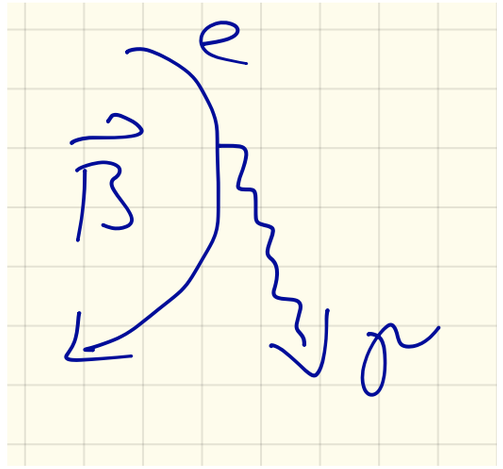

reason:
losses through synchrotron radiation at high energies

For an ensemble of electrons that are scattered randomly in all directions one could calculate the energy loss averaged over all pitch angles, which is

$$\left\langle -\frac{dE}{dt} \right\rangle = \frac{4}{3}\sigma_T c \gamma^2 U_B \qquad (2.27)$$

for relativistic electrons with $\beta \simeq 1$. Expressed in particle physics units the average energy loss becomes

$$-\frac{dE}{dt} = 3.79 \times 10^{-6} \left(\frac{B}{\text{gauss}}\right)^2 \left(\frac{E_e}{\text{GeV}}\right)^2 \text{GeV/s} \; . \qquad (2.28)$$

also inverse Compton scattering at radiation fields and bremsstrahlung on ISM

the flux of positrons and electrons

AMS Collaboration. Phys. Rev. Lett. 122 (2019) 101101

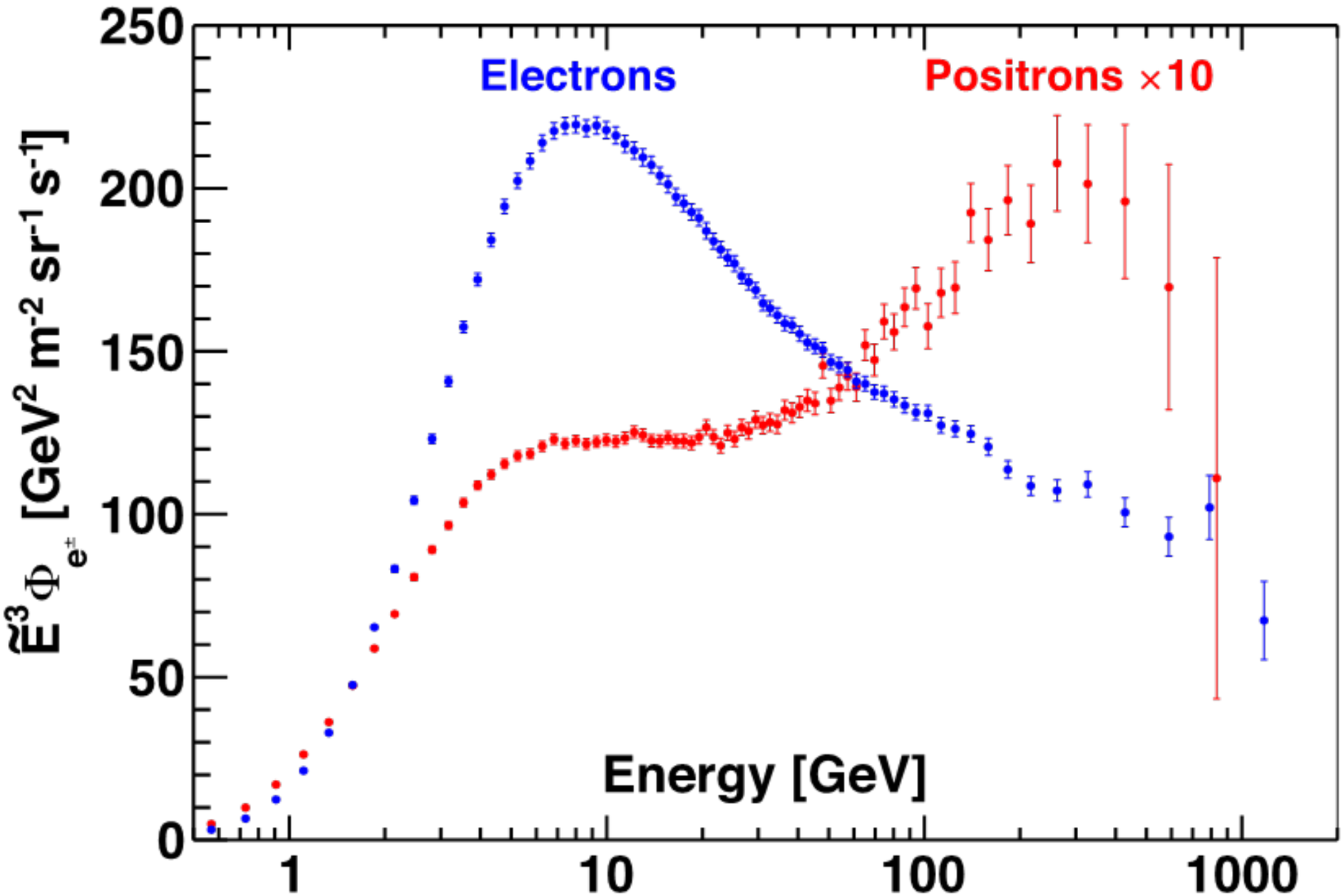

the flux of positrons

AMS Collaboration. Phys. Rev. Lett. 122 (2019) 041102

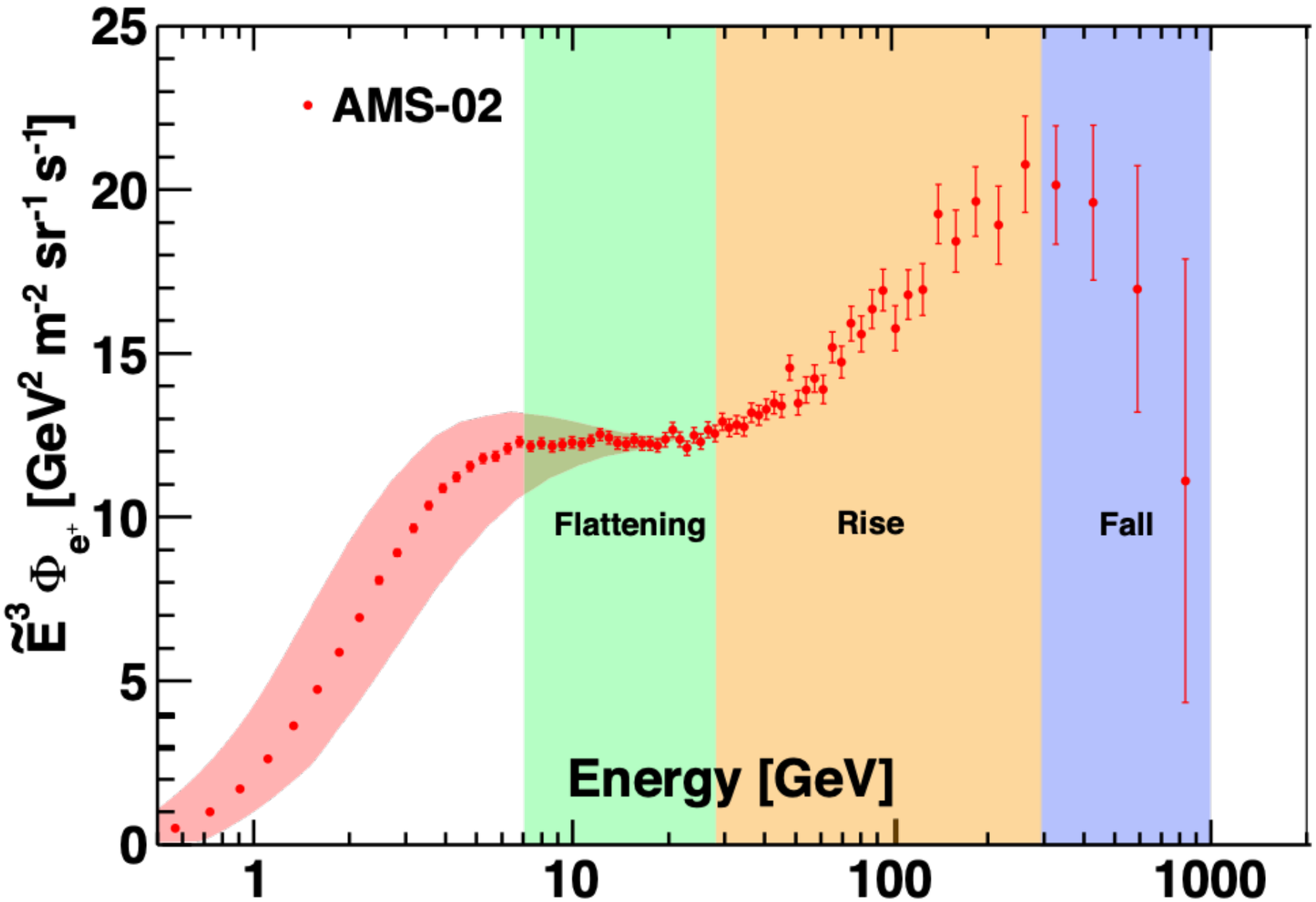

the positron excess

AMS Collaboration. Phys. Rev. Lett. 122 (2019) 041102

$$\Phi_{e^+}(E) = \frac{E^2}{\widehat{E}^2}\left[C_d(\widehat{E}/E_1)^{\gamma_d} + C_s\left(\widehat{E}/E_2\right)^{\gamma_s}\exp(-\widehat{E}/E_s)\right]$$

Diffuse term

Source term

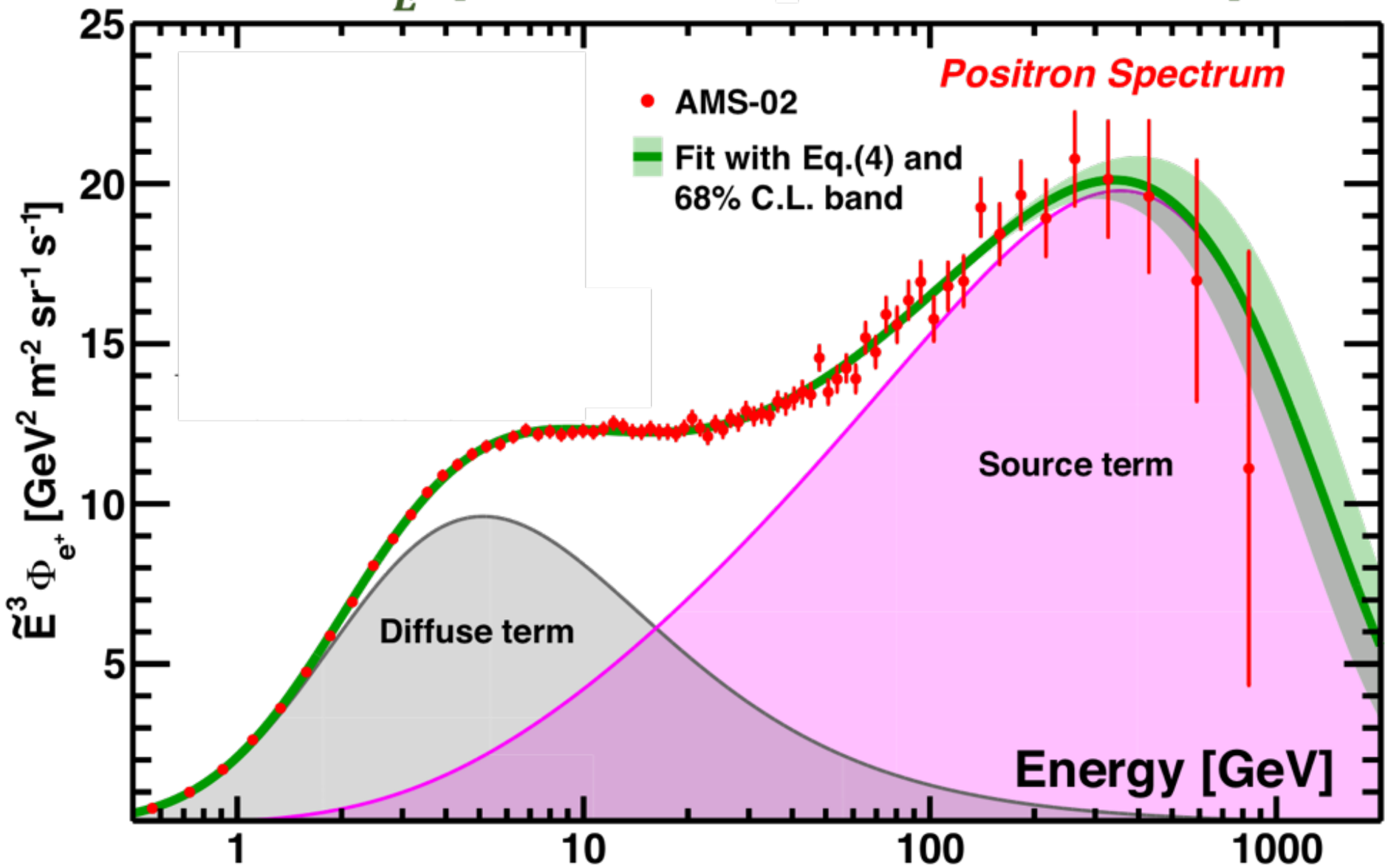

astrophysical sources (e.g. pulsars) or dark matter annihillation?

the positron excess

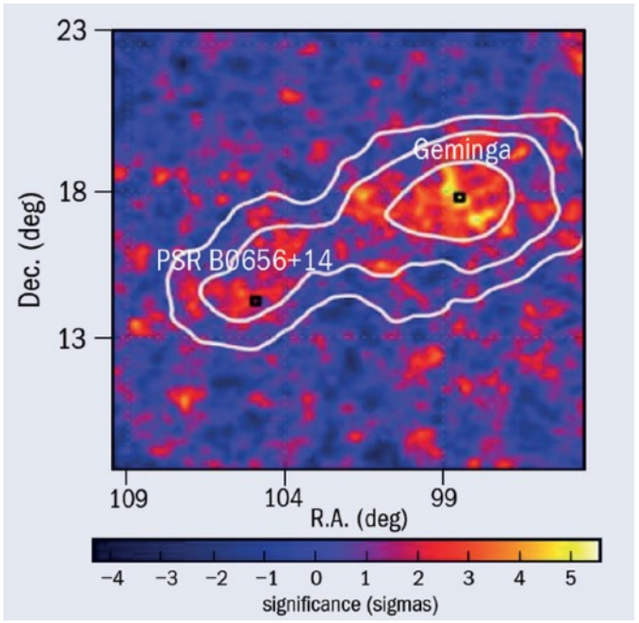

HAWC Collaboration. Science 358 (2017) 911.

- many works have claimed that the positron excess might be evidence for dark matter annihilation
- results by HAWC (High-Altitude Water Cherenkov) Observatory indicate that nearby pulsars **cannot** explain the positron excess

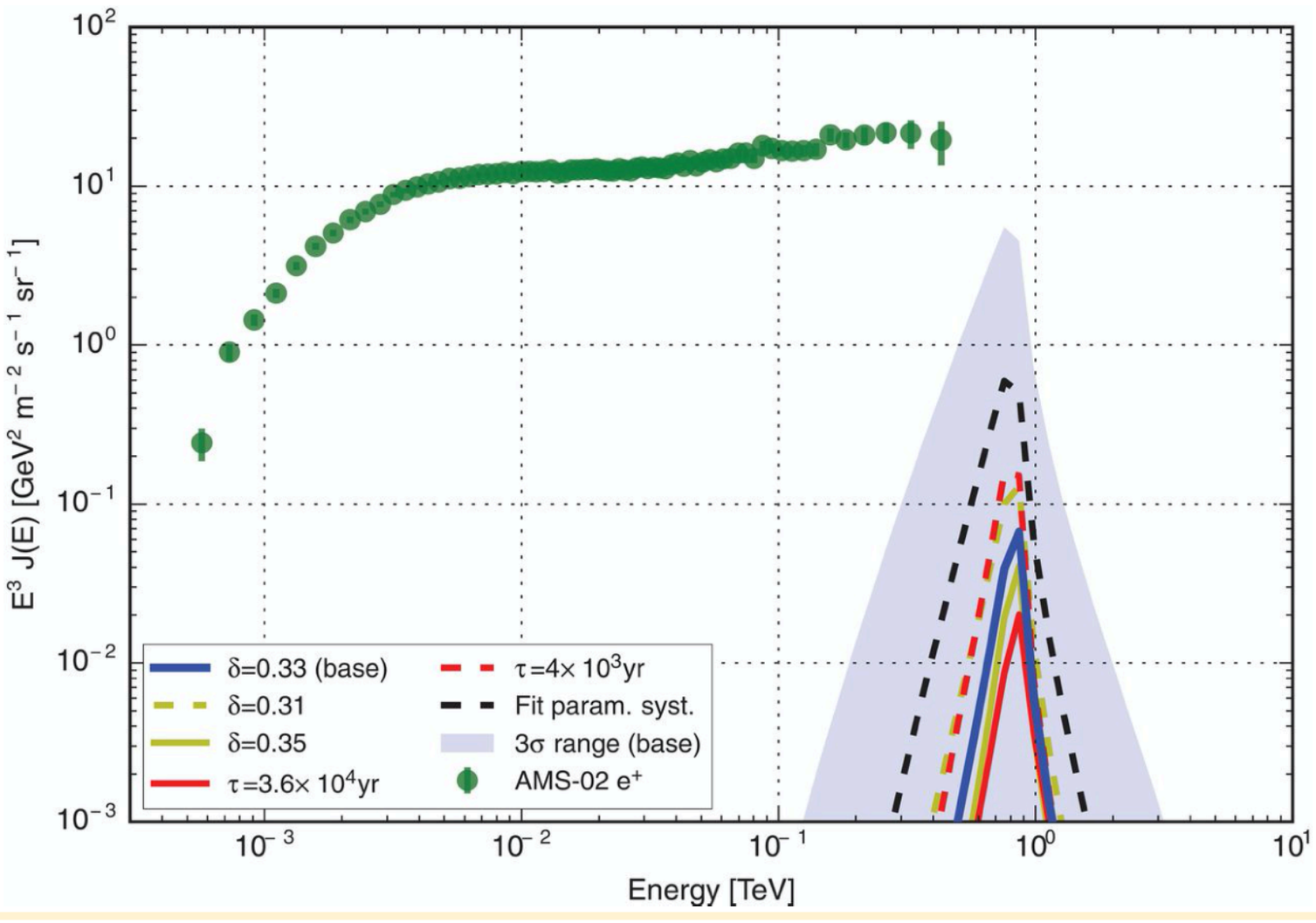

anti protons

hadronic interactions:

antiprotons are produced in proton-antiproton pairs

energy threshold 7 m_p

rapidly decreasing proton flux (power law)

—> peak at 2 GeV

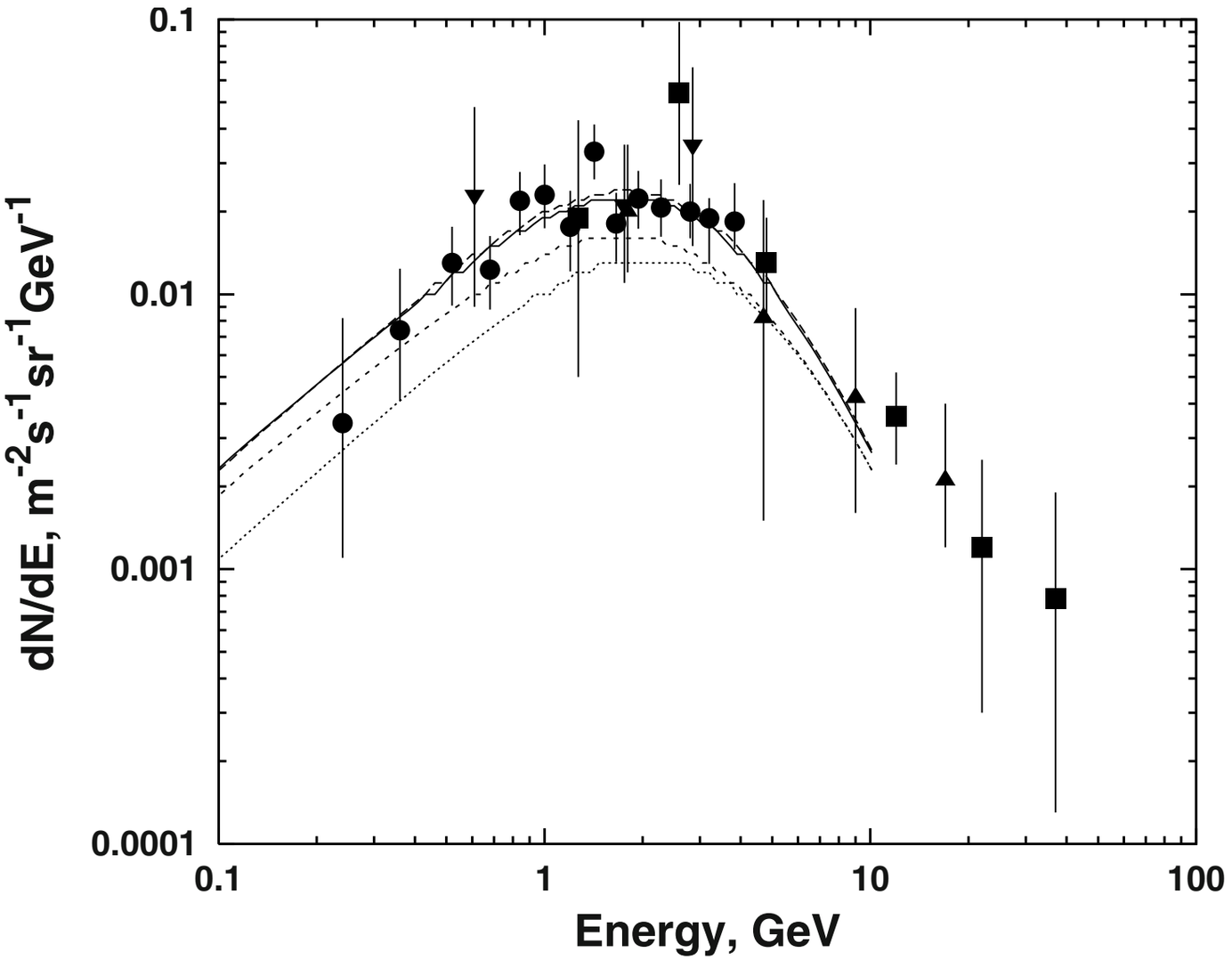

Fig. 5.18. Antiproton fluxes detected by the CAPRICE [149], squares, IMAX [157], inverted triangles, MASS [158], triangles, and the BESS [159], circles, experiments. The predictions with solar modulation for different solar epochs are from Ref. [160].

anti protons

In the leaky box approximation the equilibrium $\bar{p}$ spectrum is obtained with (4.13), where λ_{esc} is the same as for protons and λ_{int} includes annihilation and other inelastic interactions of antiprotons, all energy-dependent. The source term of antiproton production is usually divided into two parts: the antiproton production summed over all primary cosmic ray and interstellar target nuclei, and a term that accounts for the $\bar{p}$ energy loss in inelastic interactions.

If we make one more simplification and assume that no cosmic ray nuclei are created in propagation, i.e. only account for the loss of particles, the leaky box model gives the shape of the energy spectrum of a primary nucleus j after propagation as

$$N_j(E) = Q_j(E) \times \left(\frac{1}{\tau^j_{esc}(E)} + \frac{\beta c \rho_{ISM}}{\lambda^j_{int}} \right)^{-1} \quad (4.13)$$

anti protons

Figure 5.18 shows experimental data on the $\bar{p}$ flux compared to predictions [160] including the calculation of interstellar proton fluxes and solar modulation at different solar epochs. The solar modulation of the antiproton flux is different from this of protons for two reasons. The modulation at low energies is smaller than for protons, because the interstellar $\bar{p}$ spectrum increases up to about 2 GeV and $\Phi_{IS}(E_{IS})$ in (5.3) grows up to that energy and diminishes the modulation. In addition, antiprotons are negatively charged, and if the suggestion of Ref. [108] is correct their solar modulation would be different from this of protons. This last suggestion was made by Bieber et al. [160], who calculated a larger $\bar{p}/p$ ratio below 1 GeV for the epoch just before the change of the solar polarity in year 2000. This prediction was confirmed by the last measurement of the BESS group (which is not shown in Fig. 5.18).

cosmic-ray anti-protons

Perez et al. arXiv:1904.05938

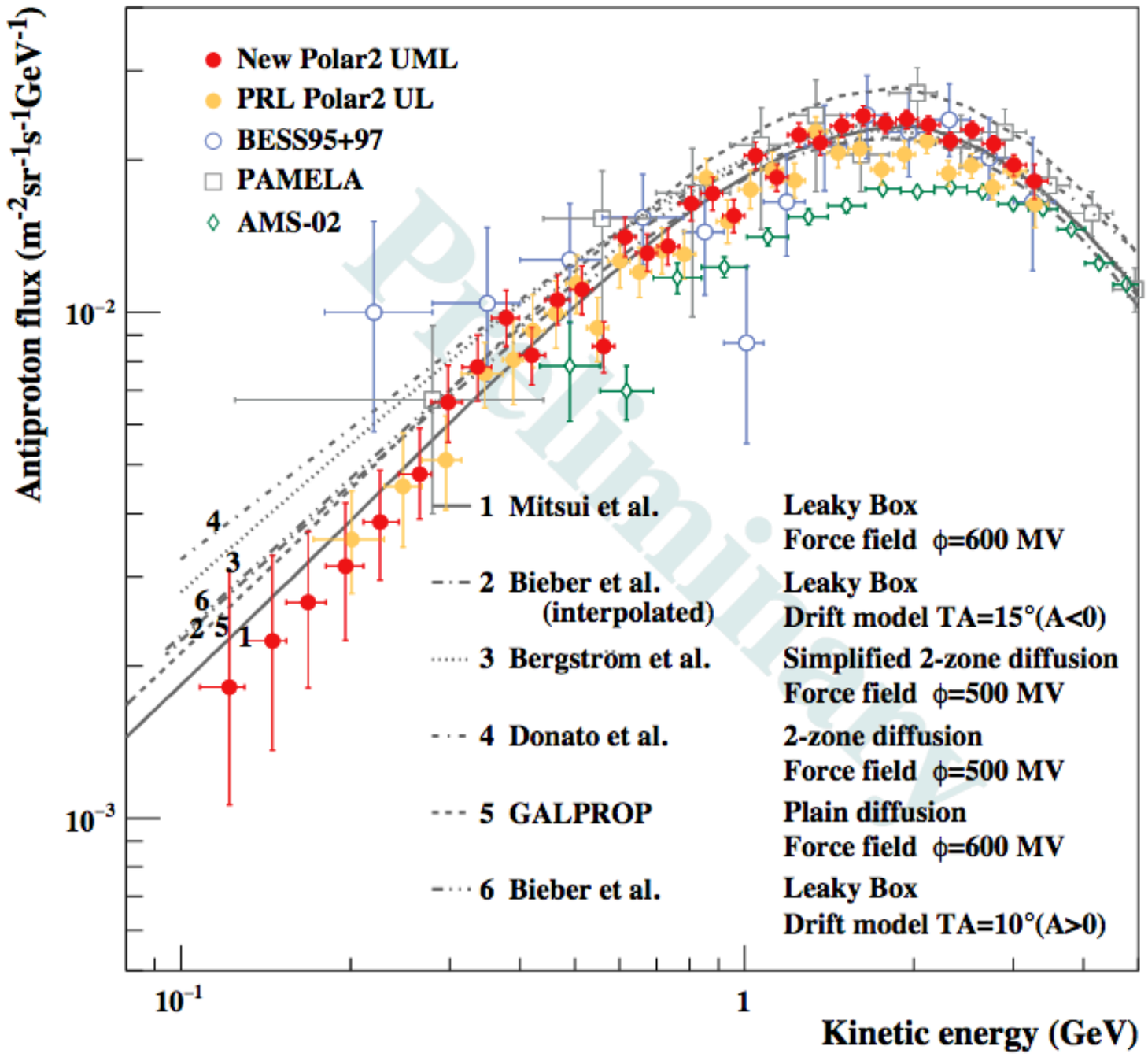

- galactic CR propagation uncertainties are represented by bands
- different dark-matter models are shown in blue, green, and grey

cosmic-ray anti-protons

AMS Collab. Phys. Rev. Lett. 117 (2016) 091103

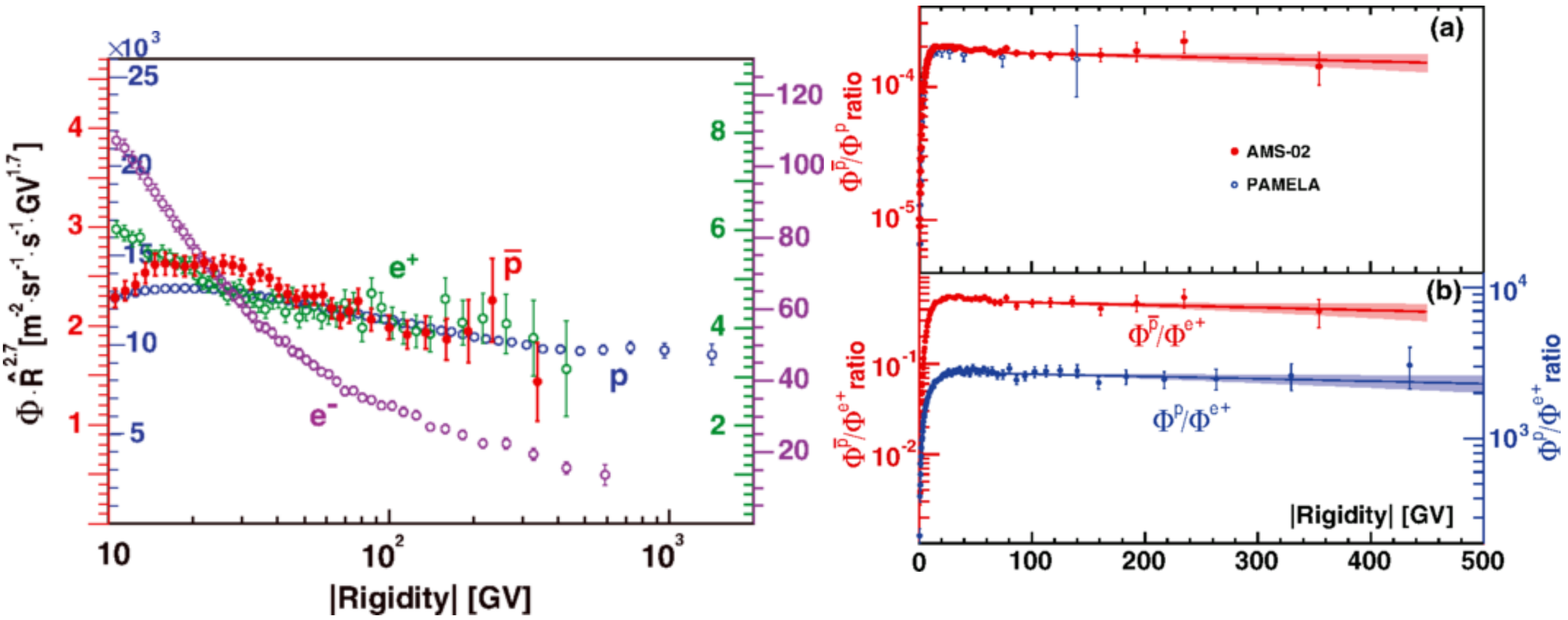

- positrons, protons, and anti-protons behave similarly above ~100 GV
- electrons behave differently

cosmic-ray anti-deuterons

Perez et al. arXiv:1904.05938

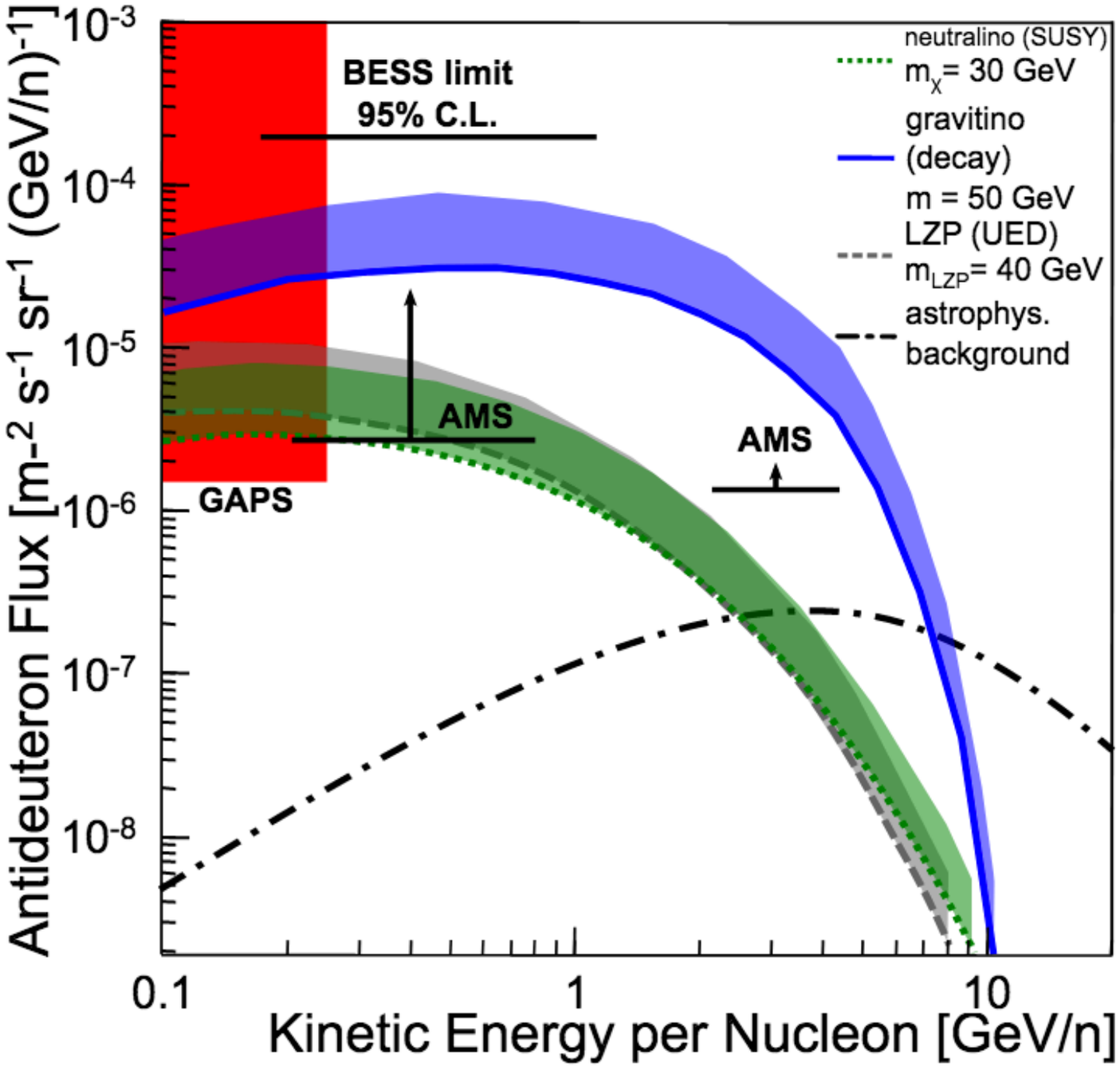

- galactic CR propagation uncertainties are represented by bands
- different dark-matter models are shown in blue, green, and grey

cosmic-ray anti-helium

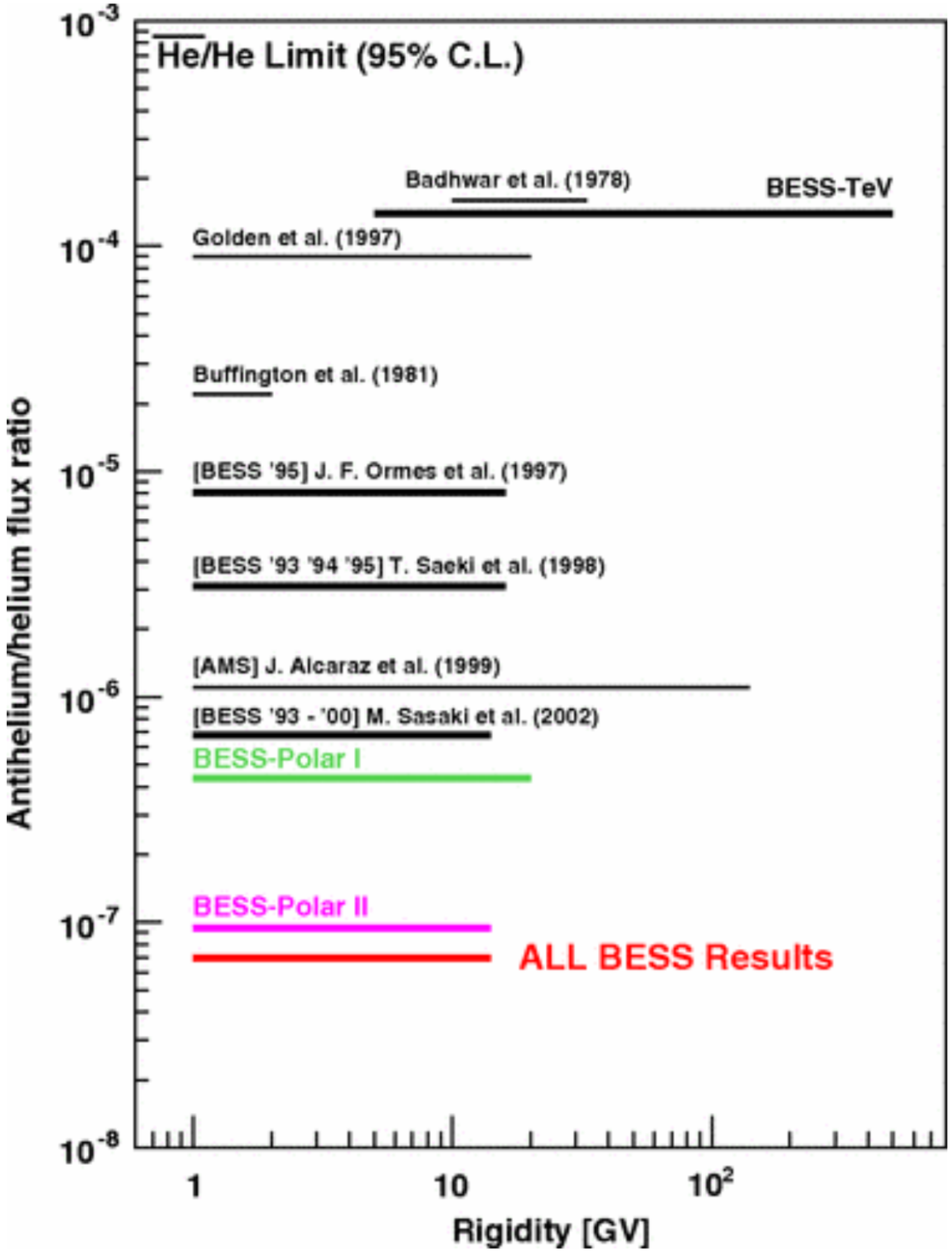

- a handful of anti-helium candidates have been detected so far (He-3, He-4)
- flux is very low, though

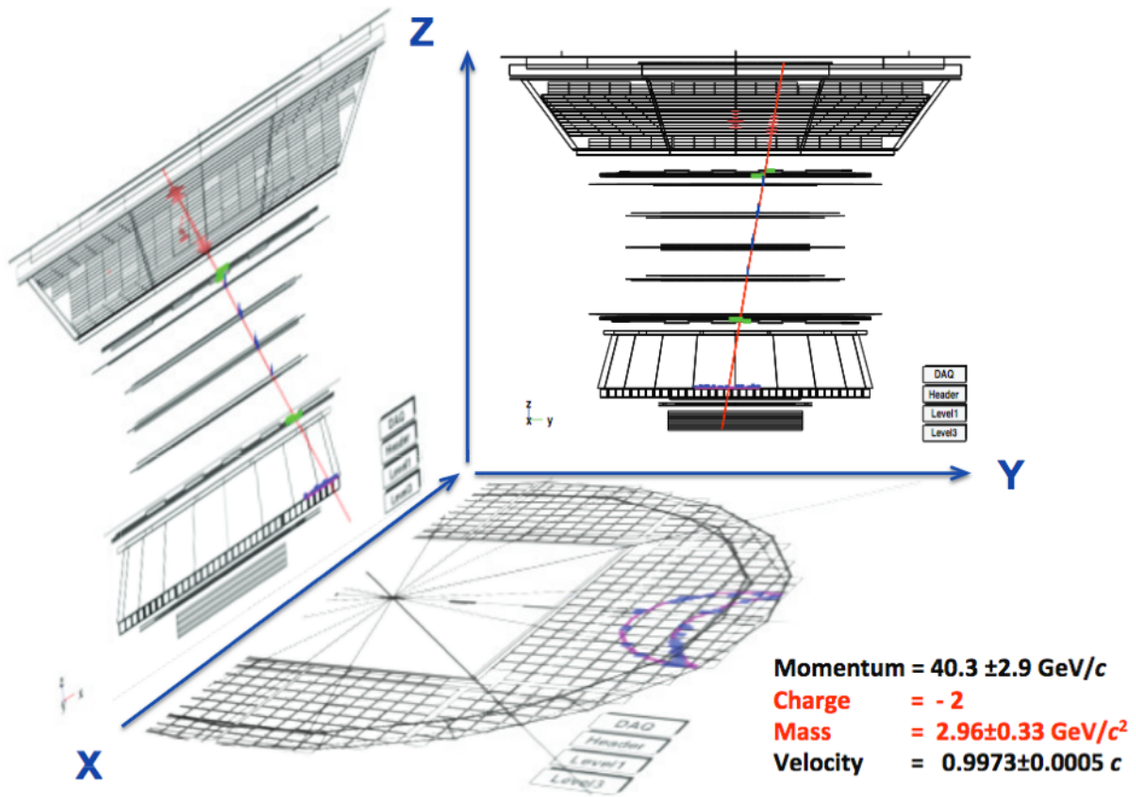

Figure 12: An antihelium candidate with a mass of ^{3}He.

today:
Stanev, chapter 6

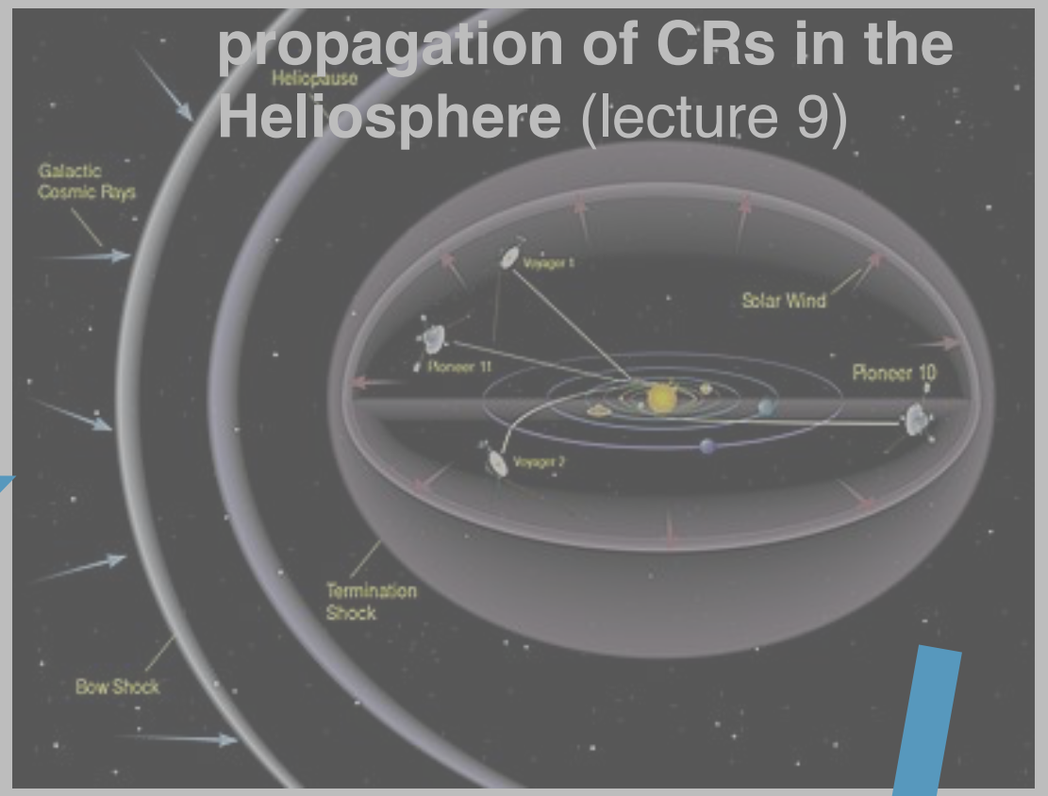

propagation of CRs in the Heliosphere (lecture 9)

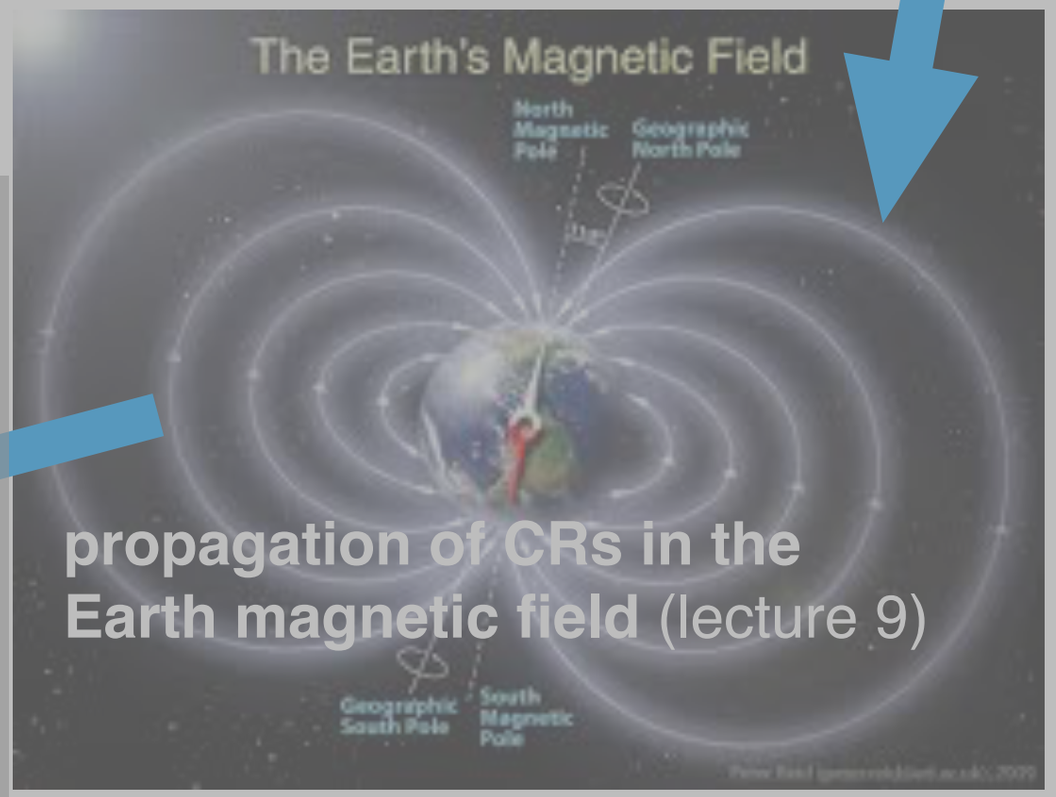

propagation of CRs in the Earth magnetic field (lecture 9)

CRs at the top of the atmosphere (lecture 10)

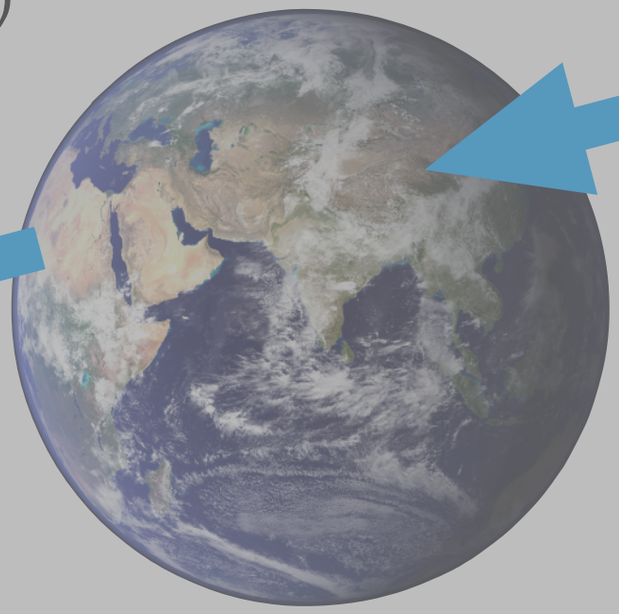

CRs underground (lecture 11)
neutrino oscillations (lecture 11+12)

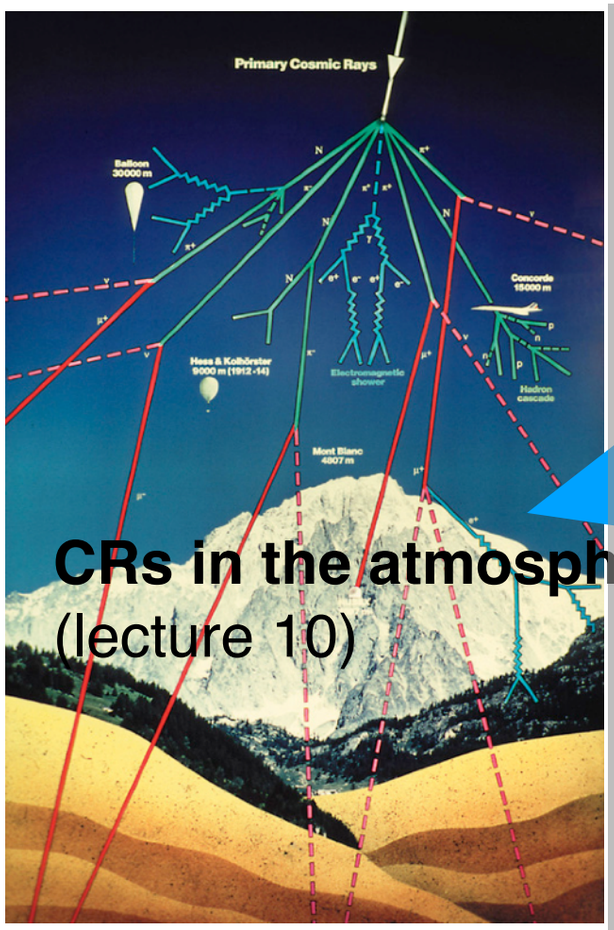

CRs in the atmosphere (lecture 10)

Cosmic rays in the atmosphere

Stanev chapter 6

Cosmic rays interact in the atmosphere and produce secondary, tertiary, etc particles.

All these particles together create a cascade —> extensive air shower.

—> calculate the fluxes of particles in the cascade, generated by a cosmic ray with mass A, charge Z, and energy E.

Such calculations would be easy if we knew exactly the properties of inelastic interactions of nucleons with medium-heavy nuclei, which provide most of the atmospheric targets. These properties are, however, not known that well.

In collider experiments, mostly central collisions are explored.

Most energy flows in forward direction.

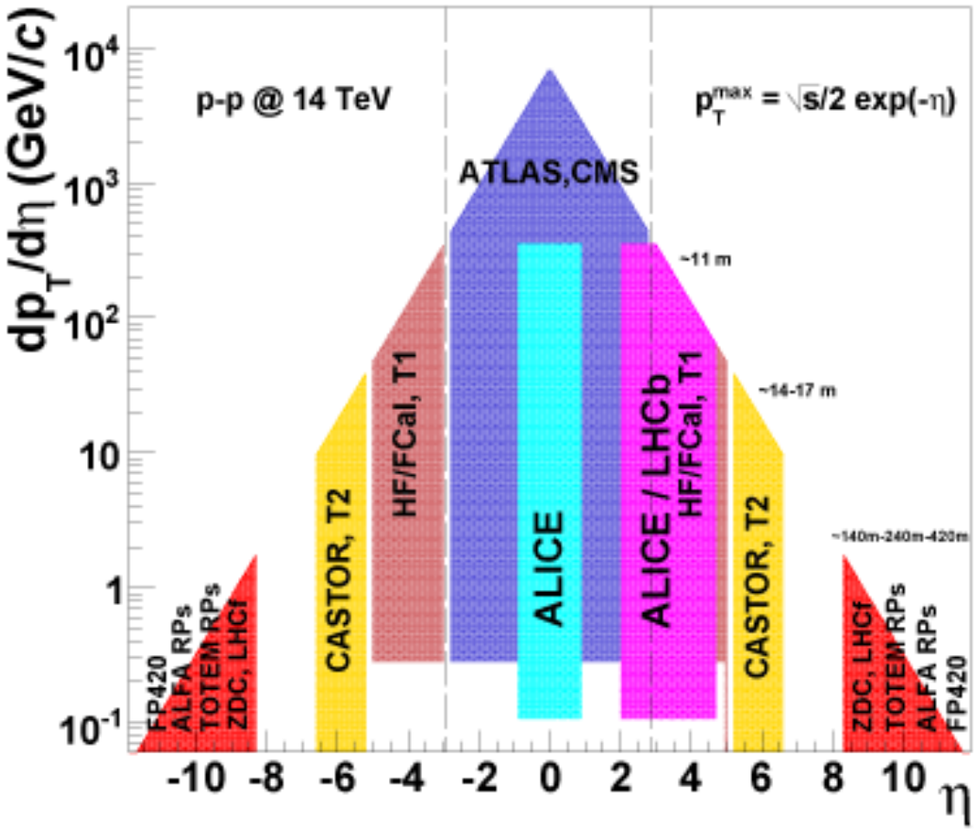

FIG. 3: Approximate p_T-η coverage of current (and proposed) detectors at the LHC (adapted from [2]).

What to be measured at colliders

multiplicity and energy flux at LHC 14TeV collisions

pseudo-rapidity; η= -ln(tan(θ/2))

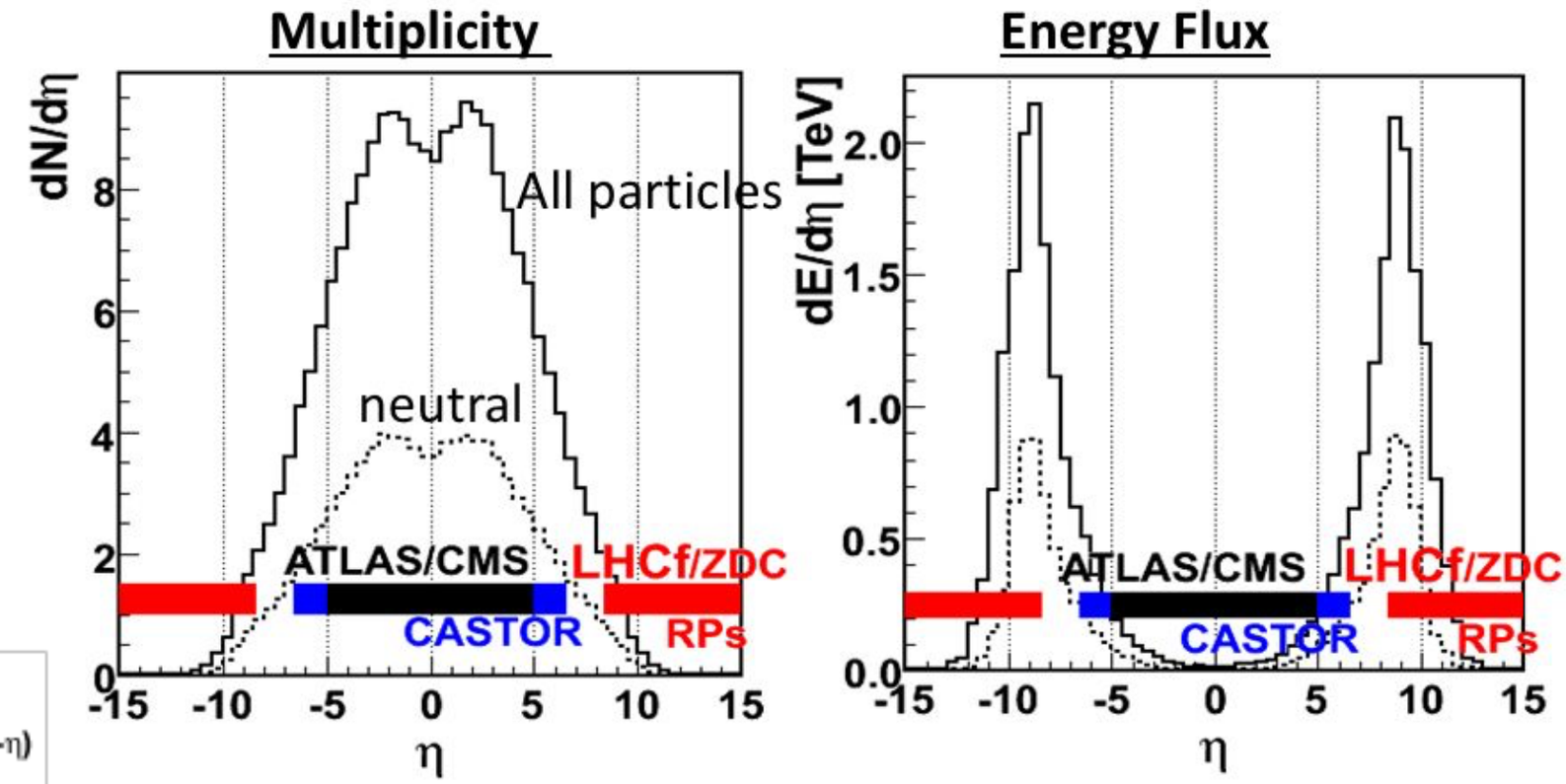

Most of the energy flows into very forward

pseudorapidity used to describe angle of particle relative to beam axis

$$\eta = -\ln\left[\tan\left(\frac{\theta}{2}\right)\right]$$

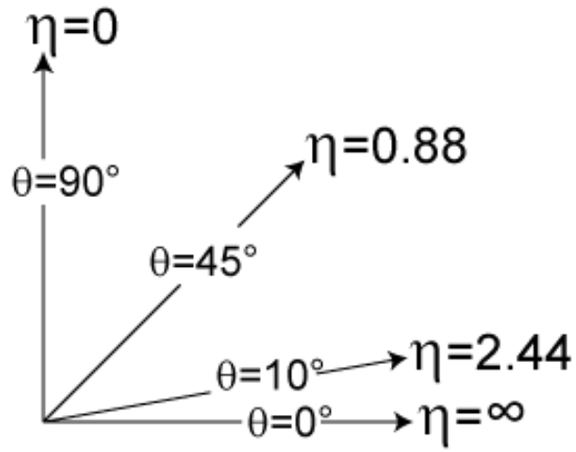

Atmospheric structure

The main parameter we want to know about the atmosphere is what is the amount of matter above any atmospheric layer, in which the primary cosmic ray particle has interacted, produced secondaries and started the air shower. This quantity is the atmospheric depth, X, measured in g/cm^2. The depth is the integral in altitude of the atmospheric density above the observation level h, i.e.

$$X = \int_h^\infty \rho(h_1)\, dh_1 \; . \tag{6.1}$$

The ratio of the atmospheric pressure ($\equiv X$) to density in the atmosphere is proportional to the temperature. If the temperature were constant, then the relation between altitude and depth would be very simple

$$X = X_o \exp(-h/h_0) \; , \tag{6.2}$$

where X_0 is the atmospheric depth at sea level (1,030 g/cm^2) and h_0 is the scale height of the atmosphere. This is true for perfect gas with constant composition that is in hydrostatic equilibrium.

h_0 ~8 km for h<5 km and ~6.4 km above

Atmospheric structure

The measurements of the altitude dependence of the temperature can be approximately fit with a two temperature dependences. The temperature decreases with altitude up to the troposphere, and is then constant. Equation (6.2) can then be used for the upper atmosphere. A fit of the US Standard Atmosphere for medium latitudes and the seasons of spring and fall gives tropospheric altitude of 11 km, average surface temperature of 15°C and temperature drop rate of 6.5°C per kilometer. M. Shibata has added to it a third layer that accounts for the increase of the temperature at very large altitudes. The altitude dependence of the atmospheric depth X then becomes:

$$\begin{aligned} \ln X &= 5.26 \ln\left[(44.34 - h)/11.86\right] \quad for\ h < 11\,\mathrm{km} \\ &= (45.5 - h)/6.34 \text{ for } 25\,\mathrm{km} > h > 11\,\mathrm{km} \\ &= 13.78 - 1.67\left[68.47 - 1.2 \times (48.63 - h)\right]^{\frac{1}{2}} \quad \text{for } h > 25\,\mathrm{km} \end{aligned} \tag{6.3}$$

All coefficients are in kilometers and the atmospheric depth X is in g/cm^2.

Atmospheric structure

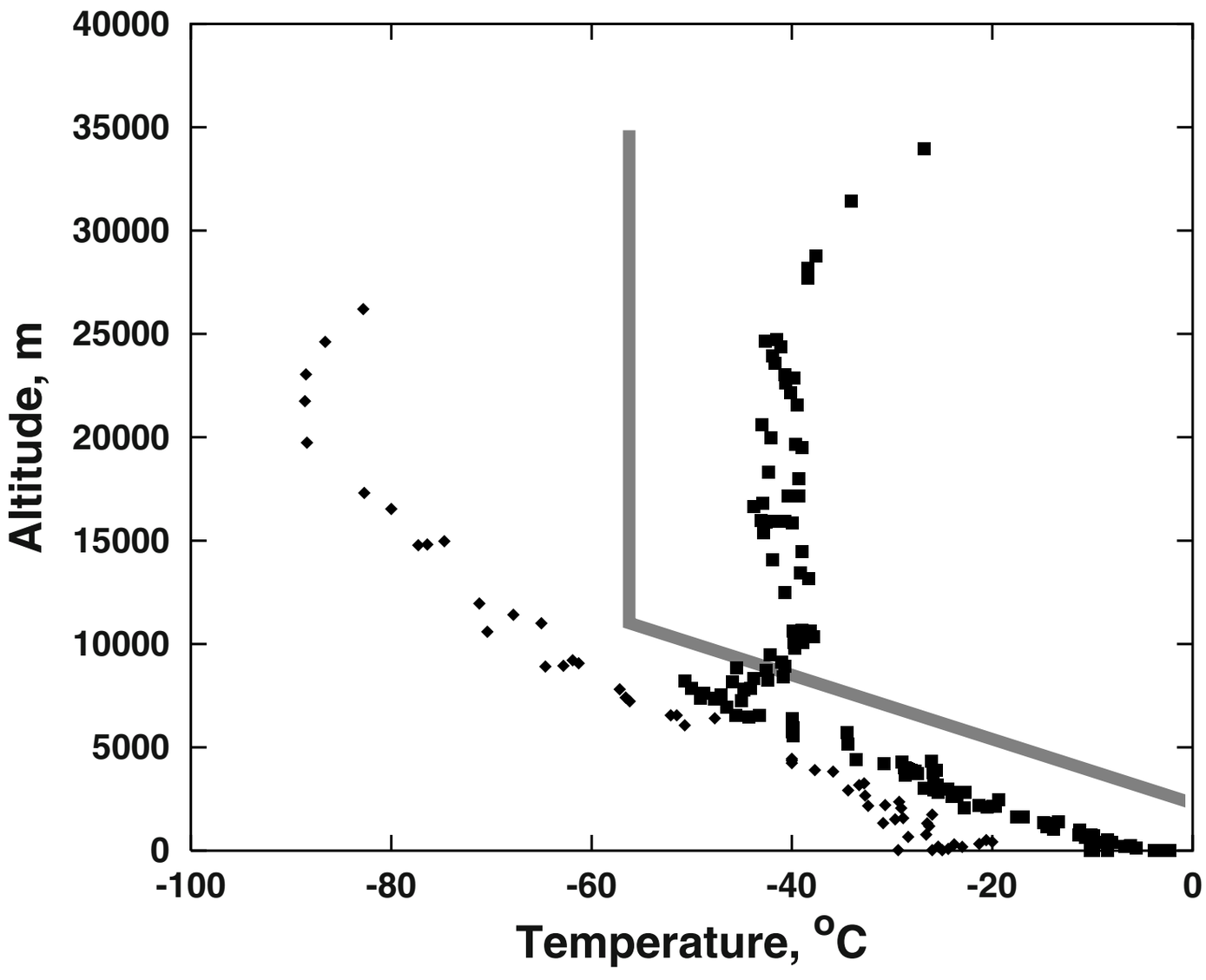

Fig. 6.2. Measurements of atmospheric temperature at McMurdo during the austral summer, squares, and winter, diamonds. The shaded line shows the assumptions of (6.3).

Atmospheric structure

All the formulae and numbers above are for the vertical direction. For zenith angles less than 60° one can scale the slant depth as $X \cos\theta$ - the flat Earth approximation. For larger angles one has to account correctly for the curvature of the Earth. This is usually done in tabular form after mapping the altitude dependence of the atmospheric density and integrating in altitude numerically along the angle. The atmospheric profile of (6.3) gives total horizontal atmospheric depth of 36,000 g/cm^2.

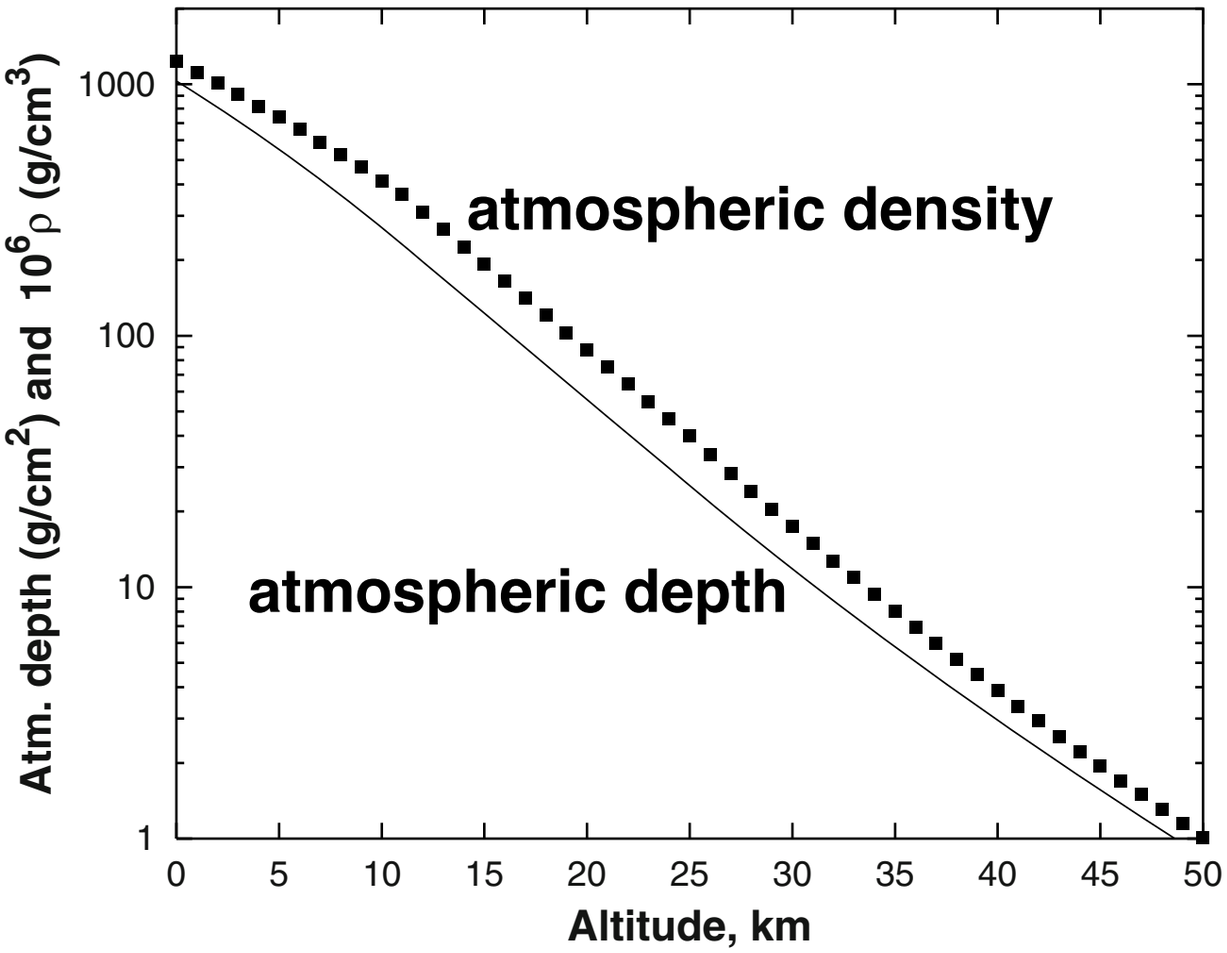

Fig. 6.1. Altitude dependence of the vertical atmospheric depth X (line), and the atmospheric density ρ (points) from the atmospheric model of (6.3)

Analytic approximations

The air shower development can be modeled analytically through the solution of transport equations similar to those of Sect. 4.3. We follow Gaisser's approach [6] in this section. The basic equation for uncorrelated[1] particle fluxes of type j at atmospheric depth X is

$$\frac{dF_j(E,X)}{dX} = -\left(\frac{1}{\lambda_j}+\frac{1}{d_j}\right)F_j(E,X)+\sum_i\int\frac{g_{ij}(E_i,E_j)}{E_i}\frac{F_i(E_i)}{\lambda_i}\,dE_i \quad (6.4)$$

where λ_j is the mean free path for inelastic interactions of a particle of type j and d_j is its decay length. The mean free path (m.f.p.) $\lambda_j \equiv A/(N_A\sigma_j)$ is the inverse of the product of the number of nuclei with mass A per gram of matter and the interaction cross-section. The average mass of an air nucleus is 14.5 and for a proton cross-section 300 mb (3×10^{-25} cm^2) we obtain $\lambda_p(air)$ of 80 g/cm^2. The mean free path λ_j is energy dependent. The decay length d_j is also expressed in g/cm^2. For zenith angles θ below 60° (in the flat Earth approximation) it is defined as

$$\frac{1}{d_j} \equiv \frac{\epsilon_j}{EX\cos\theta}\,, \quad (6.5)$$

where ϵ_j is the critical energy at which the interaction probability in the atmosphere equals the decay probability.

Analytic approximations - nucleons

Particles of energy $E \ll \epsilon_j$ always
decay and of energy $E \gg \epsilon_j$ always interact. The second term in (6.4) is the source term, which sums over the production of secondary particles j with energy E_j by particles of type i with energy E_i.

For stable particles, and when the source term in (6.4) can be neglected, the solution becomes simple [6]

$$F_j(E, X) \;=\; F_j(E, 0)\, \exp\left(-\frac{X}{\Lambda_j}\right), \tag{6.6}$$

where Λ_j is the particle absorption length and $F_j(E, 0)$ is the boundary condition, i.e. the flux of particles of type j at the top of the atmosphere. The energy spectrum of nucleons, neglecting the production of nucleon–antinucleon pairs in the atmosphere, is given by (6.6) with Λ_p defined as

$$\frac{1}{\Lambda_N} \;=\; \frac{1}{\lambda_N}\left[1 - Z_{NN}\right] \;, \tag{6.7}$$

where λ_N is the nucleon m.f.p. and Z_{NN} is the spectrum weighted moment of the nucleon production cross section by nucleons – see (4.15). To the first approximation $\gamma = 1.7$ for atmospheric processes. Λ_N than has a value of about 120 g/cm^2. See Gaisser's book [6] for tables of spectrum weighted moments and absorption lengths.

Analytic approximations - mesons

The fluxes of atmospheric mesons are much more complicated. One has to write explicitly the coupled cascade equations given in a general form by (6.4) and use the appropriate Λ and Z values. Since Λ and Z are mildly energy-dependent the solutions are useful in restricted energy range. Gaisser solves the equation for the pion fluxes in the atmosphere in the two extreme cases: for pion energy $E_\pi \gg \epsilon_\pi$ and for $E_\pi \ll \epsilon_\pi$. $\epsilon_\pi = 115$ GeV for vertical fluxes.

Neglecting decay, and with the boundary condition $\Pi(E,0) = 0$, i.e. there are no primary pions, the vertical pion flux at depth X is

$$\Pi(E,X) \;=\; F_N(E,0)\frac{Z_{N\pi}}{(1-Z_{NN})}\frac{\Lambda_\pi}{\Lambda_\pi-\Lambda_N}\left[\exp\left(-X/\Lambda_\pi\right)-\exp\left(-X/\Lambda_N\right)\right]\;, \tag{6.8}$$

where $F_N(E,0)$ is the nucleon flux on the top of the atmosphere. This flux reaches maximum at $\sim$140 g/cm^2 and then declines. Deep in the atmosphere the flux decreases as $\exp(-X/\Lambda_\pi)$.

In the low energy case, including decay, the solution requires more work and becomes

$$\Pi(E,X) \;\simeq\; F_N(E,0)\frac{Z_{N\pi}}{\lambda_N}\frac{XE}{\epsilon_\pi}\,\exp(-X/\Lambda_N)\;. \tag{6.9}$$

Pion flux in the atmosphere

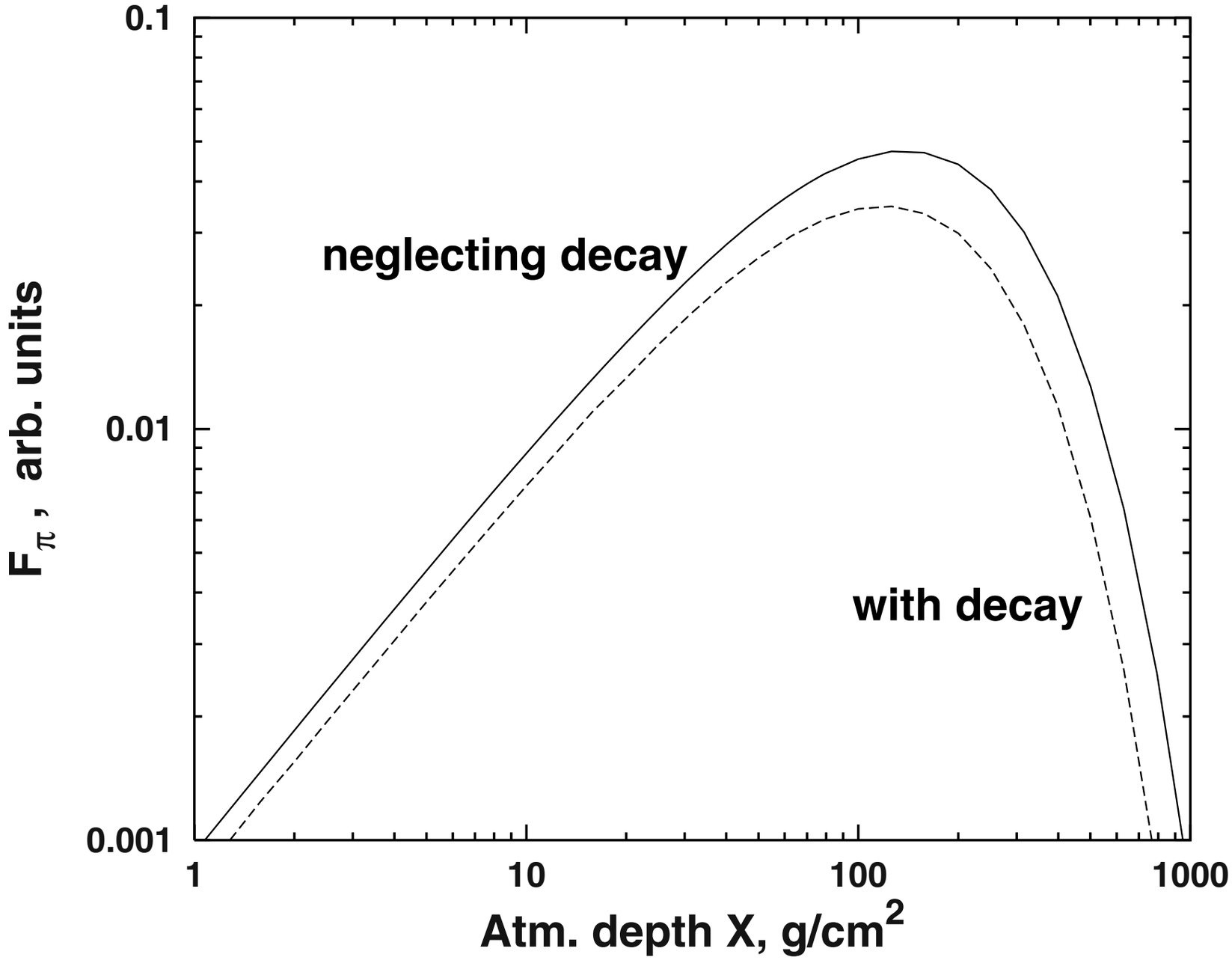

Fig. 6.3. Pion flux in the atmosphere calculated with (6.8) and (6.9) neglecting decay, solid line, and with decay, dashes. The normalization of the two curves is arbitrary, only the shape is correct.

Muons from meson decay

After calculating pion fluxes in the atmosphere (as well as the fluxes of other mesons by using the corresponding values of Λ and Z) Gaisser proceeds to calculate the fluxes created by pion decay. The first step is the calculation of muons and muon neutrinos from charged pion decays – $\pi^+ \longrightarrow \mu^+ + \nu_\mu$ and respectively $\pi^- \longrightarrow \mu^- + \bar{\nu}_\mu$. The production spectrum of the decay particles of energy E at depth X is a sum of all atmospheric decays of particles of type i that generate particles of type j.

$$P_j(E,X) = \sum_i \int_{E_{min}}^{E_{max}} \frac{dg_{ij}(E,E')}{dE} D_i(E',X)\, dE' \,, \tag{6.10}$$

where $dg_{ij}(E,E')/dE$ is the spectrum of secondaries j from decaying particles of type i with energy E'. D_i is the spectrum of decaying mesons of energy E' at depth X, which is the flux of such particles weighted by the decay probability $\epsilon_i/(E'X\cos\theta)$. E_{min} and E_{max} are the minimum and maximum energy of the decay particles determined by (2.37). For two-body pion decay the minimum muon energy $E^\mu_{min} = E_\pi(m^2_\mu/m^2_\pi) \simeq 0.57 E_\pi$ and $E^\mu_{max} = E_\pi$.

Muons from meson decay

Accounting for the two-body decays of pions and kaons and assuming a proton spectrum of $1.8E^{-2.7}$ cm^{-2} s^{-1} sr^{-1} GeV^{-1} Gaisser obtains the muon spectrum in the same units after an integration over the muon production in the whole atmosphere.

$$\frac{dN_\mu}{dE_\mu} \simeq 0.14 E_\mu^{-2.7} \left[\frac{1}{1 + \frac{1.1 E_\mu \cos\theta}{115 \text{ GeV}}} + \frac{0.054}{1 + \frac{1.1 E_\mu \cos\theta}{850 \text{ GeV}}} \right], \tag{6.11}$$

where the first term in the square brackets represents the muons from pion decay and the second one represents the muons from kaon decay. 850 GeV is the value of ϵ_K and 0.054 is the weight of the kaon contribution of the muon flux coming from the kaon production cross-section and the muon branching ratio of kaon decays. Equation (6.11) does not account for the muon energy loss and will only be correct at relatively high energy when the energy loss is only a small fraction of the muon energy.

Muons from meson decay

Equation (6.11) reveals two important features of the muon spectrum. At low energy ($E_\mu \ll \epsilon_\pi$) the muon spectrum has the shape of the primary cosmic ray spectrum, while at high energy it steepens by one power of E_μ as the thickness of the atmosphere is not big enough for pions to decay. The pion decay length $c\tau_\pi$ is 7.8 m and for $E_\pi = 1{,}000$ GeV it becomes 55.7 km, longer than the vertical extent of the atmosphere. Because of the $\cos\theta$ factor pions decay more easily in nonvertical showers and muons at large angles have a flatter energy spectrum. Note also that the contribution of kaons to the muon flux increases with the muon energy because of higher value of ϵ_K. At low energy the relative contribution of kaons is about 5% and it grows up to 27% asymptotically.

Muon energy spectrum on ground

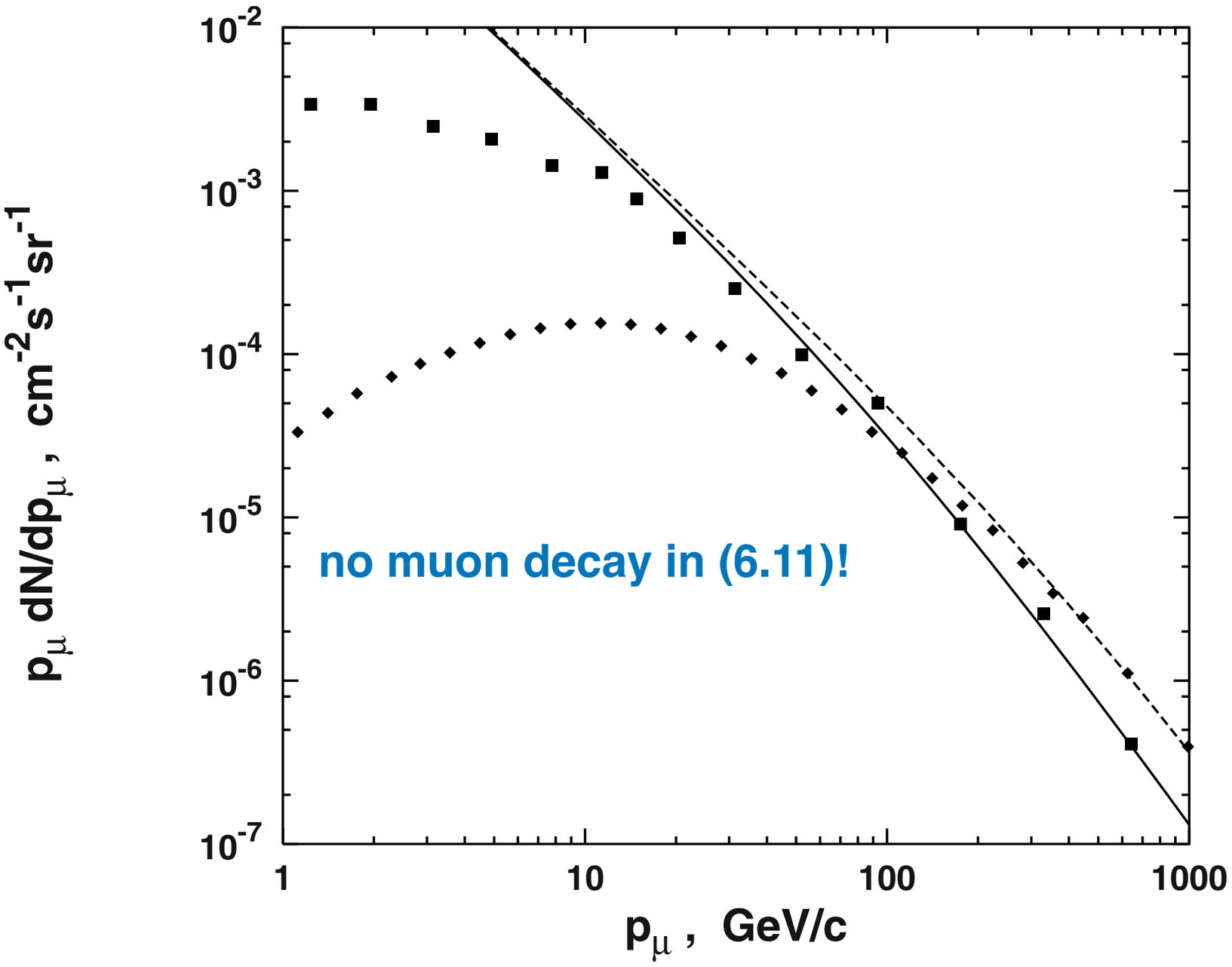

Fig. 6.4. The muon flux of (6.11) (solid line for vertical and dashed line for 75°) is compared to the vertical muon flux of Ref. [163], squares. The diamonds show the muon flux at the angle of 75° presented in Ref. [164].

Zenith angle dependance of the muon flux

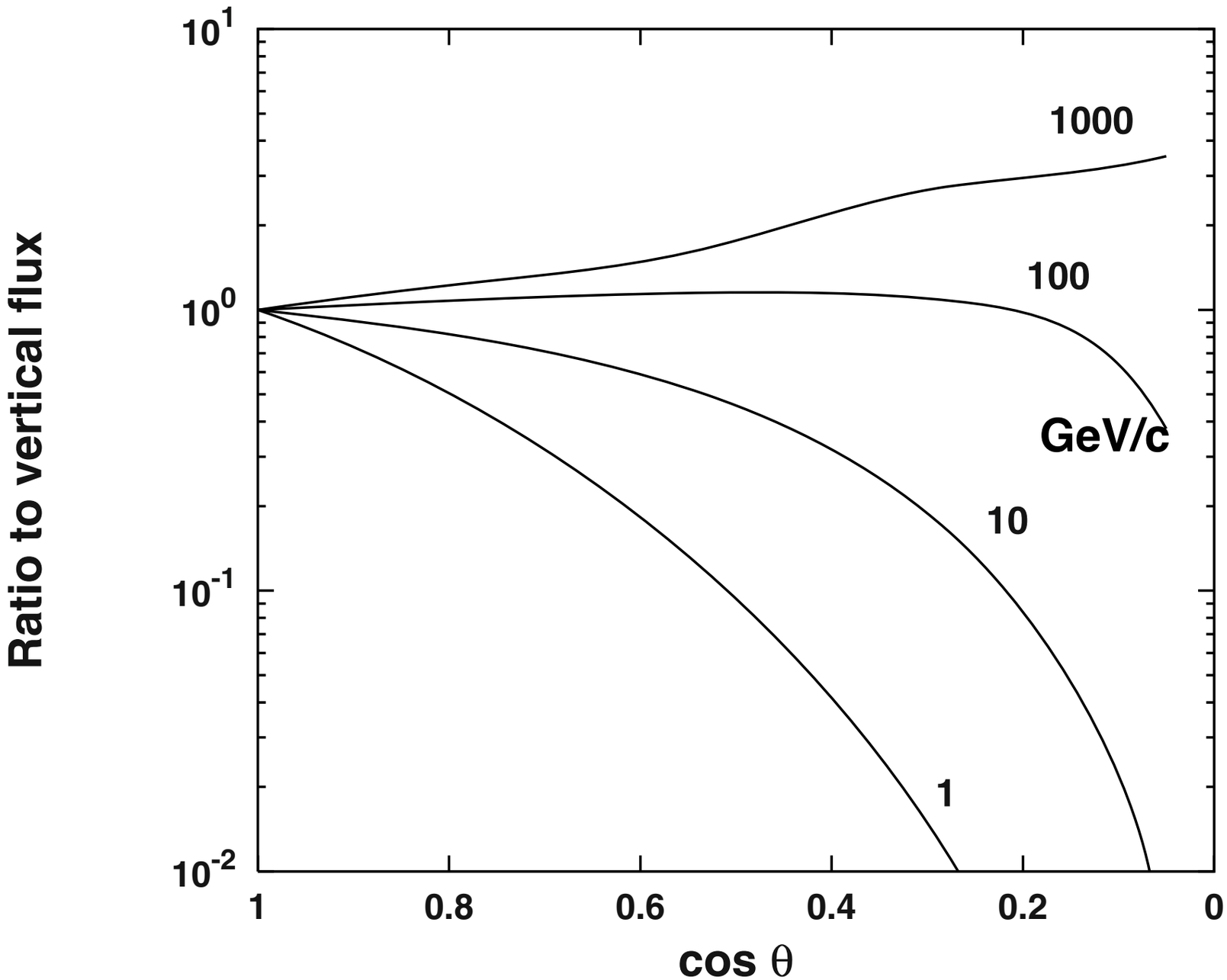

Fig. 6.5. The ratio of the inclined to the vertical muon flux as a function of the cosine of the zenith angle θ, from Ref. [165]. Muon momentum is given by each curve in GeV/c.

Muon energy spectrum at ground

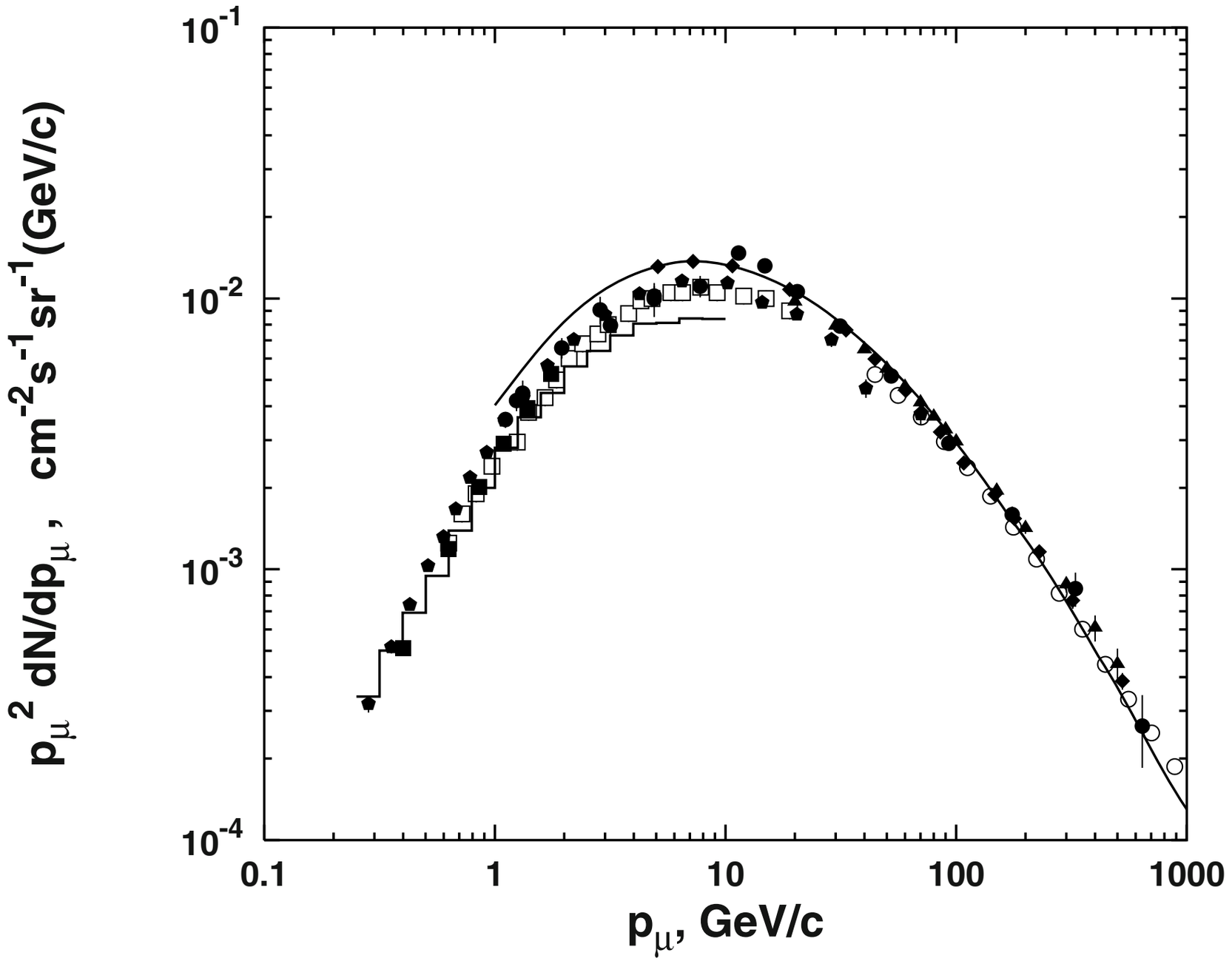

Fig. 6.6. Muon ground differential energy spectra measured by different experiments weighted by p_μ^2. See text for the references and symbols representing the data sets. The line is from Ref. [165] and the histogram, from Ref. [174].

Muon energy spectrum at ground

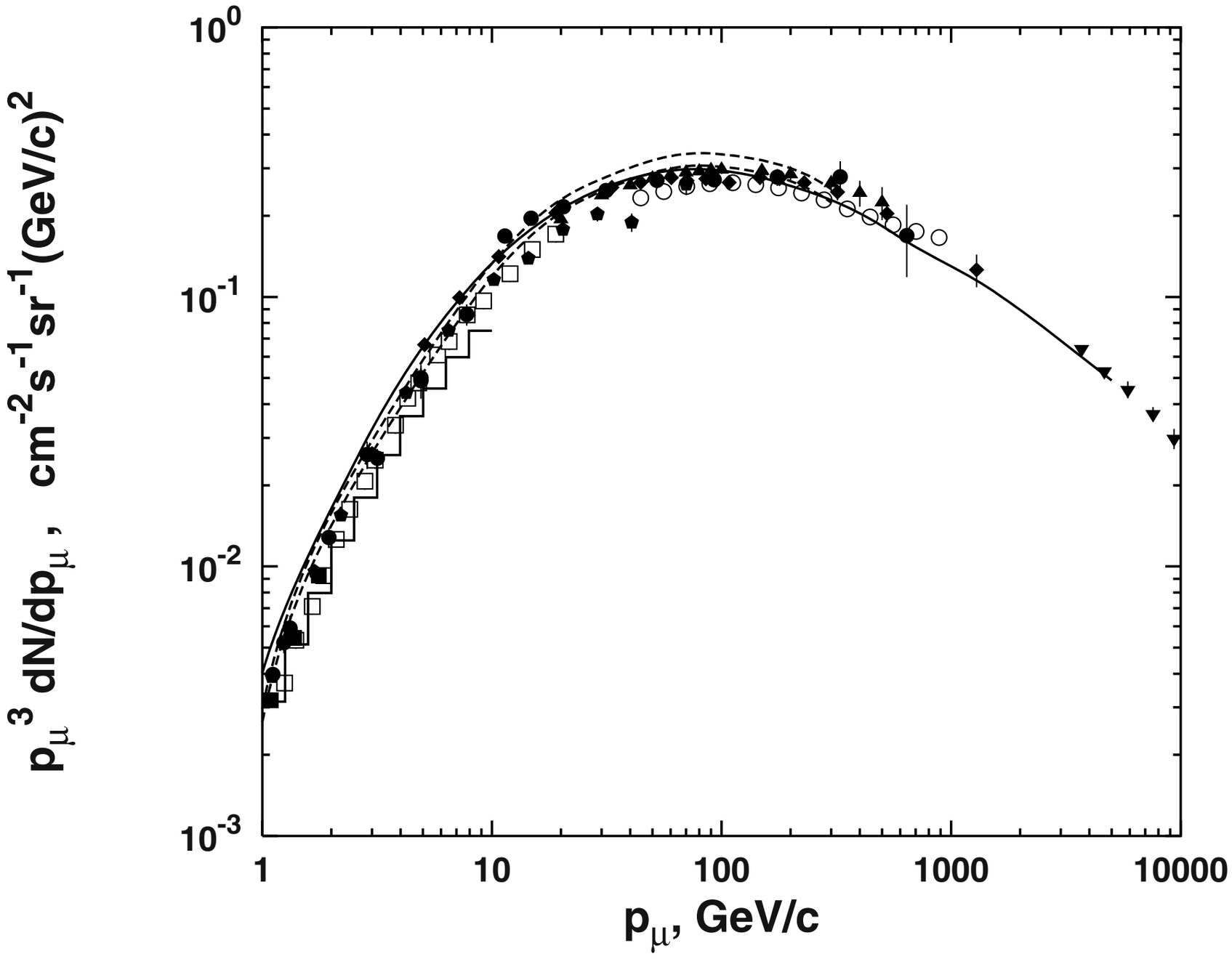

Fig. 6.7. Ground muon differential energy spectra weighted by p_μ^3. The symbols and the solid lines are the same as in Fig. 6.6. The dashed lines are the predictions of Ref. [175].

Longitudinal development of muonic component

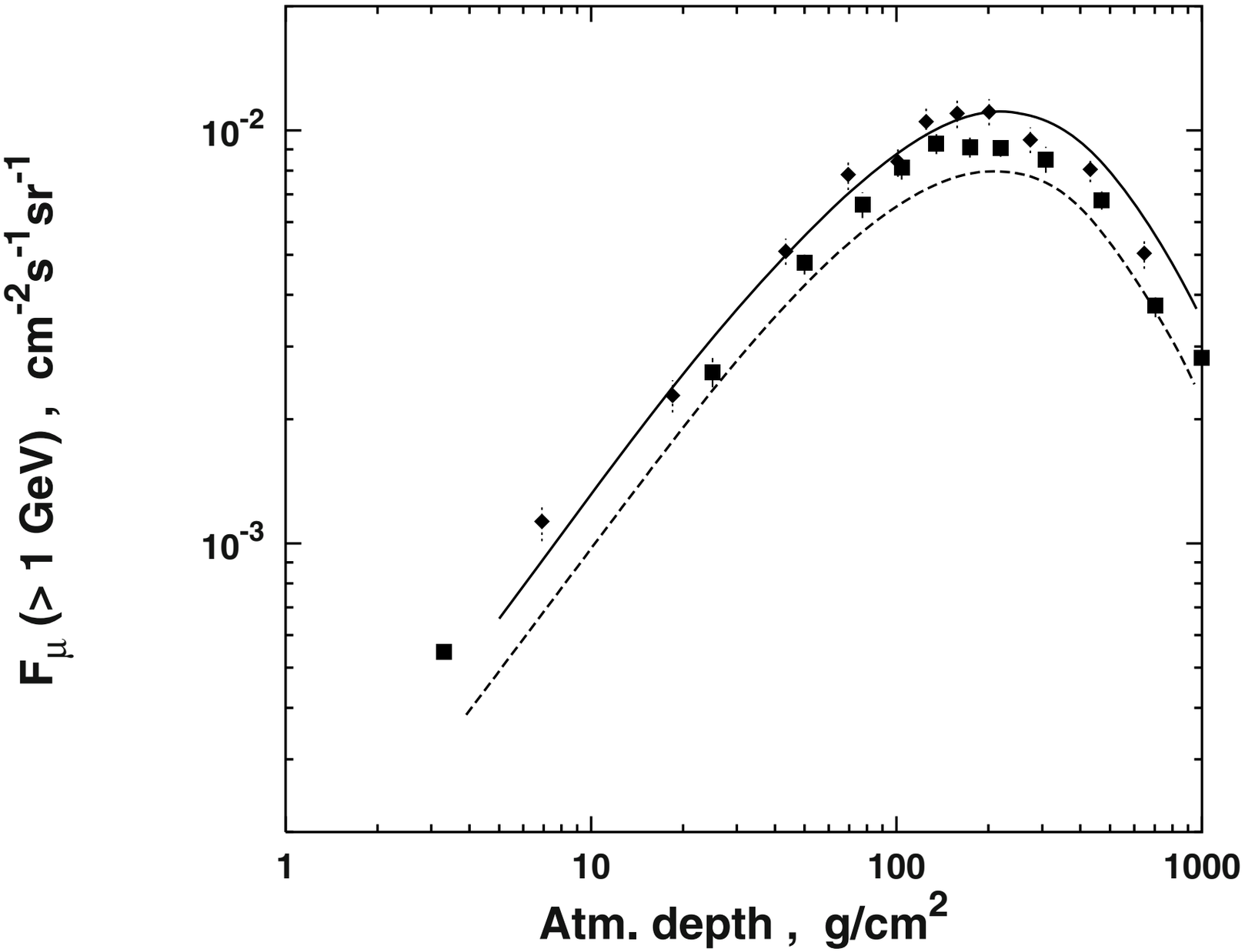

Fig. 6.8. Muon growth curve. The full squares are from Ref. [172] and the diamonds are from Ref. [176]. The predictions are from Refs. [165, 174], shown with a full and a dashed line respectively.

Muon charge ratio

Another piece of data that is of common interest is the muon charge ratio $R = F_{\mu^+}/F_{\mu^-}$. At low muon energy R is a measure of the ratio of protons to neutrons in the primary cosmic ray flux. In pp interactions the ratio of positive to negative pions in the final state is well above 1, especially among the fastest pions produced in the collision. It is related to the charge conversion probability for protons, i.e. interactions of the type $p + p \rightarrow n + p + \pi^+ + ...$ These effects are milder, but still noticeable, for interactions on air nuclei, where the target is half protons and half neutrons. The dominance of protons in the primary cosmic ray flux makes R greater than unity and the measured R values can be interpreted in terms of the average p/n ratio of the cosmic ray flux.

Muon charge ratio

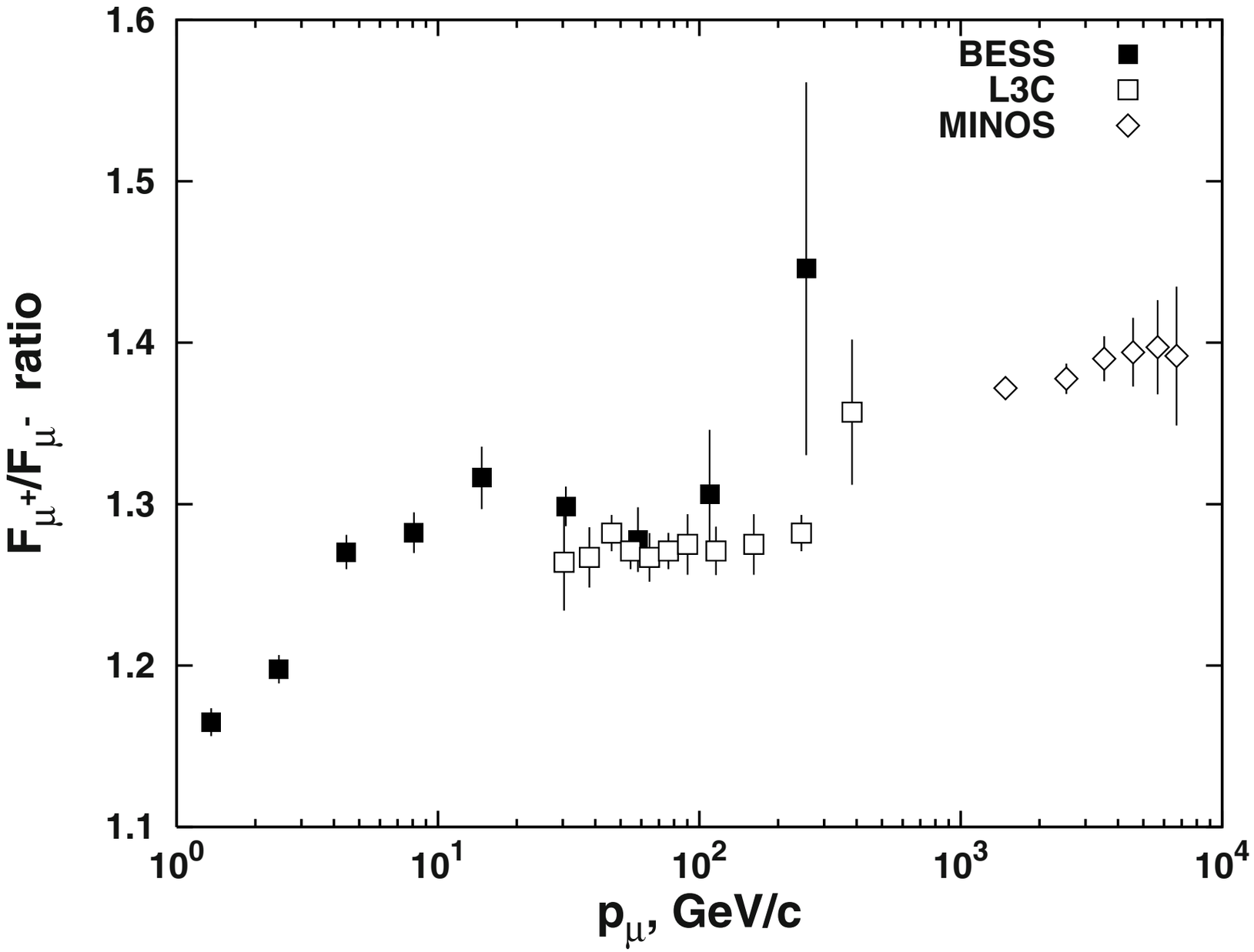

Fig. 6.9. Muon charge ratio as a function of the muon energy. The full squares are from the BESS measurement [177], the open one are from L3C [167], and the diomonds - from MINOS [178].

Muon charge ratio

At high muon energy the muon charge ratio increases. Fig. 6.9 shows the data of BESS [177], L3C [167], and MINOS [178]. R increases from about 1.2 in the GeV range to 1.4 at TeV energy. The MINOS Collaboration relates the increase of the charge ratio to the higher contribution of kaon decays. Positively charged kaons are generated much more frequently than K^- because of the $K^+\Lambda$ production.

cosmic-ray shower development in the atmosphere

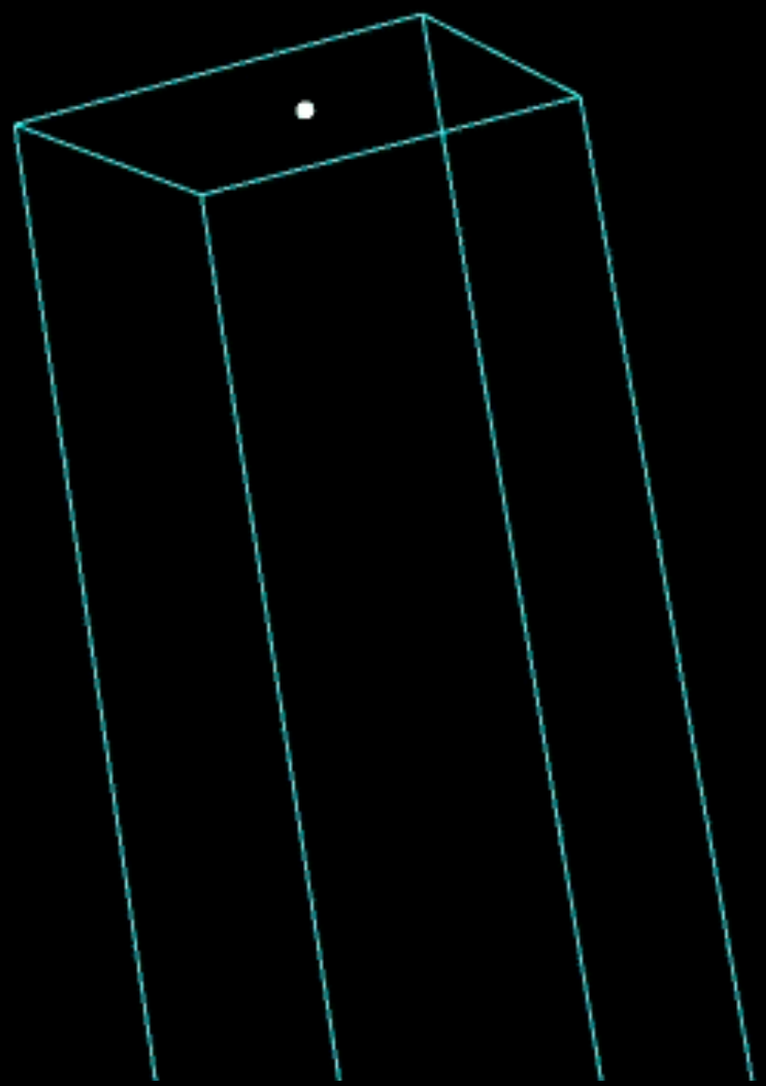

http://astro.uchicago.edu/cosmus/projects/aires/